Article

Cell Chemical Biology

S1PR3–G_{12}-biased agonist ALESIA targets cancer metabolism and promotes glucose starvation

Graphical Abstract

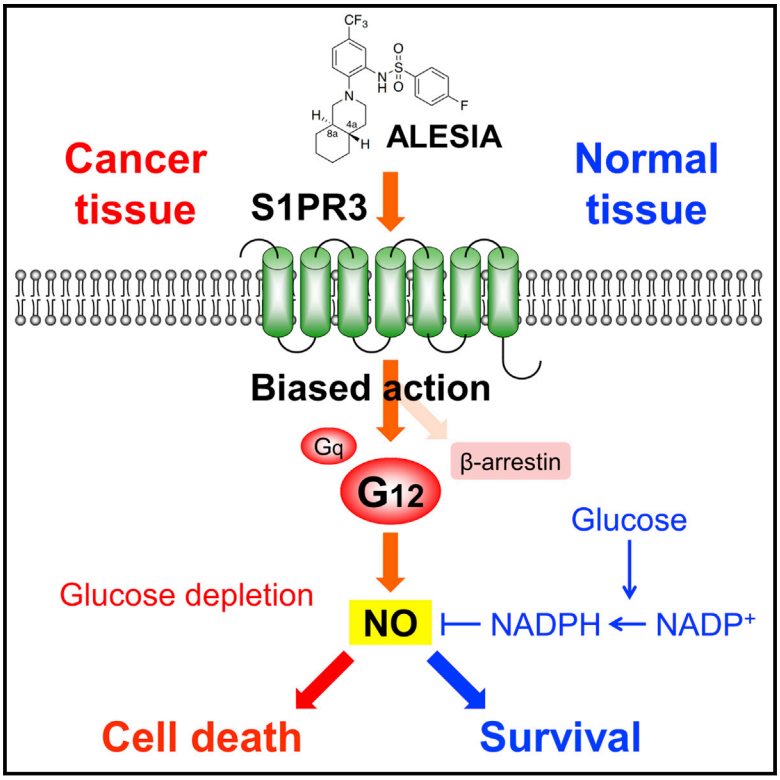

Highlights

- ALESIA is a biased agonist for S1PR3, and selectively induces G_{12} signal
- Induced G_{12} signal promotes nitric oxide production and results in glucose exhaustion
- ALESIA selectively induces apoptosis in cancer cells because of low glucose levels
- Xenograft models indicate cancer-specific glucose starvation by ALESIA

Authors

Masayasu Toyomoto, Asuka Inoue, Kei Iida, ..., Junken Aoki, Takamitsu Hosoya, Masatoshi Hagiwara

Correspondence

hagiwara.masatoshi.8c@kyoto-u.ac.jp

In Brief

Toyomoto et al. demonstrate that ALESIA is a type of biased agonist targeting the S1PR3–G_{12} signaling pathway that can induce cancer-specific glucose starvation. This discovery highlights the possible existence of an endogenous biased ligand that modulates signaling in four major families of heterotrimeric G protein.

Toyomoto et al., 2021, Cell Chemical Biology *28*, 1132–1144
August 19, 2021
https://doi.org/10.1016/j.chembiol.2021.01.004

CellPress

CellPress

Cell Chemical Biology

Article

S1PR3–G_{12}-biased agonist ALESIA targets cancer metabolism and promotes glucose starvation

Masayasu Toyomoto,[1,2] Asuka Inoue,[3] Kei Iida,[4] Masatsugu Denawa,[4] Isao Kii,[1,5] Francois Marie Ngako Kadji,[3] Takayuki Kishi,[3] Dohyun Im,[6] Tatsuro Shimamura,[6] Hiroshi Onogi,[1,7] Suguru Yoshida,[8] So Iwata,[6] Junken Aoki,[3,9] Takamitsu Hosoya,[8] and Masatoshi Hagiwara[1,10,*]

[1]Department of Anatomy and Developmental Biology, Graduate School of Medicine, Kyoto University, Kyoto 606-8501, Japan
[2]Department of Drug Discovery for Lung Diseases, Graduate School of Medicine, Kyoto University, Kyoto 606-8501, Japan
[3]Laboratory of Molecular and Cellular Biochemistry, Graduate School of Pharmaceutical Sciences, Tohoku University, Miyagi 980-8578, Japan
[4]Medical Research Support Center, Graduate School of Medicine, Kyoto University, Kyoto 606-8501, Japan
[5]Laboratory for Drug Target Research, Integrated Bioscience Division, Institute of Agriculture, Shinshu University, Nagano 399-4598, Japan
[6]Department of Cell Biology, Graduate School of Medicine, Kyoto University, Kyoto 606-8501, Japan
[7]KinoPharma, Inc., Tokyo 103-0023, Japan
[8]Laboratory of Chemical Bioscience, Institute of Biomaterials and Bioengineering, Tokyo Medical and Dental University, Tokyo 101-0062, Japan
[9]Department of Health Chemistry, Graduate School of Pharmaceutical Sciences, The University of Tokyo, Tokyo 113-0033, Japan
[10]Lead contact
*Correspondence: hagiwara.masatoshi.8c@kyoto-u.ac.jp
https://doi.org/10.1016/j.chembiol.2021.01.004

SUMMARY

Metabolic activities are altered in cancer cells compared with those in normal cells, and the cancer-specific pathway becomes a potential therapeutic target. Higher cellular glucose consumption, which leads to lower glucose levels, is a hallmark of cancer cells. In an objective screening for chemicals that induce cell death under low-glucose conditions, we discovered a compound, denoted as ALESIA (Anticancer Ligand Enhancing Starvation-induced Apoptosis). By our shedding assay of transforming growth factor α in HEK293A cells, ALESIA was determined to act as a sphingosine-1-phosphate receptor 3–G_{12}-biased agonist that promotes nitric oxide production and oxidative stress. The oxidative stress triggered by ALESIA resulted in the exhaustion of glucose, cellular NADPH deficiency, and then cancer cell death. Intraperitoneal administration of ALESIA improved the survival of mice with peritoneally disseminated rhabdomyosarcoma, indicating its potential as a new type of anticancer drug for glucose starvation therapy.

INTRODUCTION

Malignant tumors reprogram metabolic pathways to support the acquisition and maintenance of their malignant properties (DeBerardinis and Chandel, 2016). The classic example is the Warburg effect or aerobic glycolysis (Warburg, 1956). Glycolysis is a physiological response to hypoxia in normal tissues, but cancer cells constitutively take up glucose and produce lactate regardless of oxygen availability (Koppenol et al., 2011). Thus, addiction to glucose is a hallmark of tumor tissues, which allows distinguishing between cancer cells and normal tissues (Hanahan and Weinberg, 2011). Actually, excessive consumption of glucose in cancers is the basis for ^{18}fluoro-2-DG-positron emission tomography (FDG-PET) imaging (Hay, 2016; Heiden et al., 2009).

Increased aerobic glycolysis in cancer cells provides sufficient energy, as well as promoting their proliferation by providing the required building blocks (Hay, 2016; Heiden et al., 2009; Pavlova and Thompson, 2016). Thus, targeting the glycolytic pathway is a reasonable approach as a cancer treatment strategy. In the glycolysis pathway, hexokinase, phosphofructokinase, glucose transporters, pyruvate dehydrogenase kinase, lactate dehydrogenase, pyruvate kinase, and fatty acid synthesis/fatty acid oxidation are potential targets of anticancer therapeutics (Gill et al., 2016). However, anticancer drugs focusing on the enzymes of the glycolytic pathway have been clinically unsuccessful (Vander Heiden and DeBerardinis, 2017). Clinical trials for 2-deoxy-D-glucose (2DG) as a glycolytic inhibitor for cancer were suspended owing to damage to non-cancerous cells (Gill et al., 2016; Vander Heiden and DeBerardinis, 2017; Raez et al., 2013), whereas those for lonidamine, a hexokinase II inhibitor, were suspended because of the lack of therapeutic efficacy or severe complications in patients (Berruti et al., 2002; Pacini et al., 2000).

Considering the lack of clinical response to the inhibitors of glycolytic enzymes, we attempted to screen anticancer agents targeting cancer-specific metabolic pathways with a different strategy and discovered an interesting molecule, ALESIA (Anticancer Ligand Enhancing Starvation-induced Apoptosis).

RESULTS

Discovery of a compound targeting glucose-addicted cancer cells

Glucose levels in malignant tumor tissues of patients are lower than those in the surrounding normal tissues because of the Warburg effect (Hirayama et al., 2009). To identify chemicals with potent cytotoxicity under only low-glucose conditions, we established a cell-based screening system using MIA PaCa-2 cells, a pancreatic carcinoma cell line, because pancreatic cancer is one of the most malignant neoplasms. Although the average blood glucose level is approximately 1 g/L, the glucose concentrations in cancer tissues are only 2%–8% of that volume (Hirayama et al., 2009). Thus, we defined low-glucose condition as that having 0.05 g/L, whereas normal glucose level was 1.0 g/L in our experiments. We focused on a hit compound 414 (c414; Figures S1A and S1B), which suppressed cell proliferation more effectively at low-glucose conditions than normal-glucose conditions. For its further characterization, we mainly used HeLa cells, a cervical carcinoma cell line, because they were more susceptible to c414 than MIA PaCa-2 cells (Figures S1C and S1D). Treatment with c414 suppressed the growth of HeLa cells in low-glucose medium on day 1 but not those in the normal-glucose medium (Figures S1E and S1F). When the medium was not replaced for 4 days, c414 suppressed HeLa cell growth even in normal-glucose conditions (Figure S1F). Next, we compared the effects of c414 on healthy and cancerous cells under normal-glucose condition. The viability of normal human dermal fibroblasts (NHDFs) was unaffected by c414 (Figure 1A), whereas that of HeLa cells was significantly suppressed in a dose-dependent manner on day 3 (Figure 1B). The treated HeLa cells underwent apoptosis, as indicated by TUNEL assay (Figures 1C and 1D).

Next, we evaluated the anti-tumor potency of c414 using a panel of 66 human tumor cell lines (Table S1). The cancer panel analysis was conducted only under normal-glucose conditions. MIA PaCa-2 survived with the maximum dose of c414 and the half maximal inhibitory concentration (IC_{50}) was more than 10 μM. BxPC-3 cells were more sensitive to c414 than MIA PaCa-2 among pancreatic cancer cells. AU-565 (breast cancer) and SR (lymphoma) cells were as sensitive to c414 as BxPC-3, whereas A-204 (rhabdomyosarcoma) cells were the most susceptible (Table S1). This indicates that c414 induces apoptosis in a cell-type-dependent manner. Subsequently, we searched for genes that had segregated values of expression level between the c414-response and non-response groups from the RNA sequencing (RNA-seq) database (Ghandi et al., 2019) by nonparametric analysis, exploring the cellular factors that affect the vulnerability to c414. Specifically, we extracted 53 cancer cells included in both the RNA-seq data (CCLE_RNAseq_rsem_genes_tpm_20180929.txt.gz) published by the Cancer Cell Line Encyclopedia (CCLE) and our cancer panel analysis, and selected genes that were expressed in any of the 53 cells (selected 44,123 genes from 57,820 genes). We performed a Mann-Whitney U test (Wilcoxon rank-sum test) on four types of c414-sensitive cells (A-204, AU-565, BxPC-3, and SR) and 49 types of c414-insensitive cells. After p- to q-value conversion by the Benjamini and Hochberg (BH) method, genes were checked in order of the lowest q value. Consequently, the top four genes with large differences in expression levels were all non-coding RNA, but their expression values were insignificant. Next, we listed up genes that are downregulated in at least one of the c414-sensitive cancer cells, searched for a pathway that these genes are commonly involved in by Metascape (Zhou et al., 2019), and found that at least one of the related genes to fatty acid metabolism was downregulated in all c414-sensitive cancer cells (Figures S1G and S1H).

To identify the anticancer mechanism of c414, we analyzed the transcriptomes of HeLa and MCF-7, a breast cancer cell line, and compared the differential gene expressions with or without c414 treatment. We found that the expression of thioredoxin-interacting protein (*TXNIP*), an oxidative stress-responsive gene (Zhou et al., 2010), was specifically suppressed by c414 treatment in both cell lines (Figures 1E and S2A–S2C). The decrease in TXNIP expression was confirmed both at the mRNA and protein levels in HeLa cells treated with c414 (Figures S2D, S2E, and 1F). TXNIP is ubiquitously expressed in various cells and is involved in cellular redox homeostasis by inhibiting the reducing activity of thioredoxin (Benhar et al., 2009). The decrease in TXNIP levels indicated that c414 contributed to the generation of oxidative stress, thereby causing apoptosis (Figures 1C and 1D). Thus, we examined the production of reactive oxygen species (ROS) using aminophenyl fluorescein (APF) fluorescent dye and 5-(and-6)-chloromethyl-2′,7′-dichlorodihydrofluorescein diacetate, acetyl ester (CM-H_2DCFDA; Figures 1G and S2F) and nitric oxide (NO) with 4-amino-5-methylamino-2′,7′-difluorofluorescein (DAF-FM) diacetate probe (Figure 1H). Treatment with c414 increased NO levels in HeLa cells but did not affect ROS (Figures 1G and 1H).

ALESIA results in NO production and glucose starvation

As the compound c414 from the employed chemical library was racemic, we prepared both isomers and examined their effects on HeLa cells. After a 3-day treatment, D-c414 and L-c414 increased to 186% and 500%, respectively, in mean fluorescence intensity of DAF-FM compared with the solvent (dimethylsulfoxide: DMSO) treatment (Figure 2A). The caspase-3 (an apoptosis marker) activation rates by DMSO, D-c414, and L-c414 treatment were 4.7%, 9.1%, and 18.0%, respectively (Figure 2B). Comparing the number of viable cells on days 3 and 4, L-c414 significantly reduced the number of cells (Figure 2C). The differences in the ability of the two c414 enantiomers to promote NO production and induce apoptosis suggested that L-c414 is specifically bound to a target molecule involved in these processes. Carboxy-2-phenyl-4,4,5,5-tetramethylimidazoline-1-oxyl-3-oxide (cPTIO), an NO scavenger, and N^G-nitro-L-arginine methyl ester (L-NAME), an NO synthase (NOS) inhibitor, both suppressed L-c414–induced caspase-3 activation (Figure 2D). Additionally, to examine the effect of L-c414 on proliferating cancer cells, we conducted clonogenic cell survival assays (Franken et al., 2006). The NOS inhibitor L-NAME also canceled the effect of L-c414 in the clonogenic cell survival assay (Figures 2E and 2F). NADPH is utilized by NOS for NO

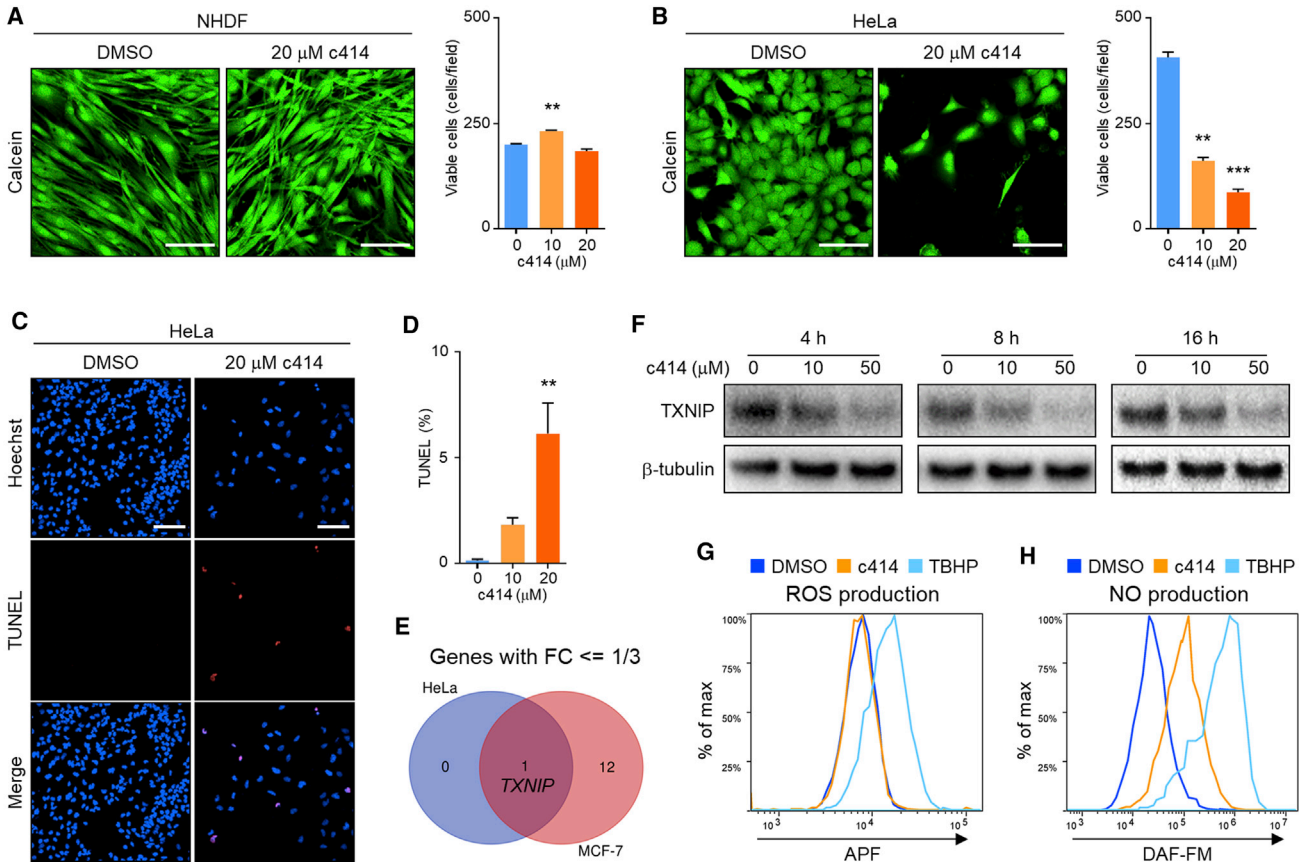

Figure 1. Discovery of a compound targeting cancer cell metabolism

(A–D) NHDFs (A) and HeLa cells (B–D) were treated with c414 for 3 days and analyzed using calcein staining (A and B) and TUNEL assay (C and D).

(E) RNA-seq transcriptome analysis of HeLa and MCF-7 cells treated with DMSO or 10 μM c414 for 6 h. Venn diagram showing downregulated genes by c414 treatment. Fold change (FC) ≤ 1/3.

(F) Immunoblot analysis of thioredoxin-interacting protein (TNXIP) and β-tubulin in HeLa cells.

(G and H) ROS (G) and NO (H) production in HeLa cells treated with 20 μM c414 for 3 days or with the ROS-generating agent *tert*-butyl hydroperoxide (TBHP; 100 μM) for 2 h. In (A)–(D), scale bars correspond to 100 μm. Error bars are expressed as SEM (n = 3). **p < 0.01, ***p < 0.001 (Tukey's test, compared with DMSO control).

synthesis (Alderton et al., 2001) and by NADPH-thioredoxin oxidoreductase (TrxR) in cellular defense against oxidative stress (Benhar et al., 2009). Thus, we assessed the amount of NADPH in HeLa cells treated with L-c414. As expected, the cellular NADPH levels were remarkably decreased after a 2-day treatment (Figure 2G). Subsequently, we explored whether an irreversible TrxR inhibitor myricetin promotes the cell-killing potency of L-c414 in clonogenic cell survival assay (Figures 2H and 2I) and expectedly observed the inhibition of TrxR-enhanced responses to L-c414. Cells consume glucose for NADPH production via the pentose-phosphate pathway (DeBerardinis and Chandel, 2016; Hay, 2016; Pavlova and Thompson, 2016). We also measured the glucose levels in the culture medium of HeLa cells. The glucose levels were markedly decreased in the presence of L-c414 (Figure 2J), whereas that in the culture medium of non-cancerous cells was considerably less pronounced (Figure 2K). In the experiments comparing NHDFs and HeLa cells, we started the culture with the same cell number (4,000 cells/well), counted the number of cells, and measured the residual glucose amount in the culture medium a day after L-c414 treatment. The glucose consumption rate per cell of HeLa cells was more than double that of NHDF (Figure S2G). L-c414 treatment promoted glucose consumption in both cell lines, of which the glucose consumption rate in HeLa cell line amounted to three times more that of NHDF treated with DMSO. These observations indicated that L-c414 induced glucose starvation and killed cancer cells. Therefore, we named L-c414 ALESIA (Figure 2L).

Starvation of nutrients promotes autophagy in mammalian cells (Mizushima et al., 2010). As ALESIA causes glucose depletion, we next tested whether it induces autophagy using immunoblot and immunofluorescence of microtubule-associated protein 1A/1B-light chain 3 (LC3; Figures 3A–3D). Notably, ALESIA increased LC3-phosphatidylethanolamine conjugate (LC3-II), a molecular marker of autophagy, in HeLa cells. Additionally, to examine the cellular response toward ALESIA, we conducted clonogenic cell survival assays in both normal- and low-glucose conditions. As expected, ALESIA markedly reduced the survival of HeLa cells in the low-glucose state compared with that in normal glucose (Figures 3E–3H).

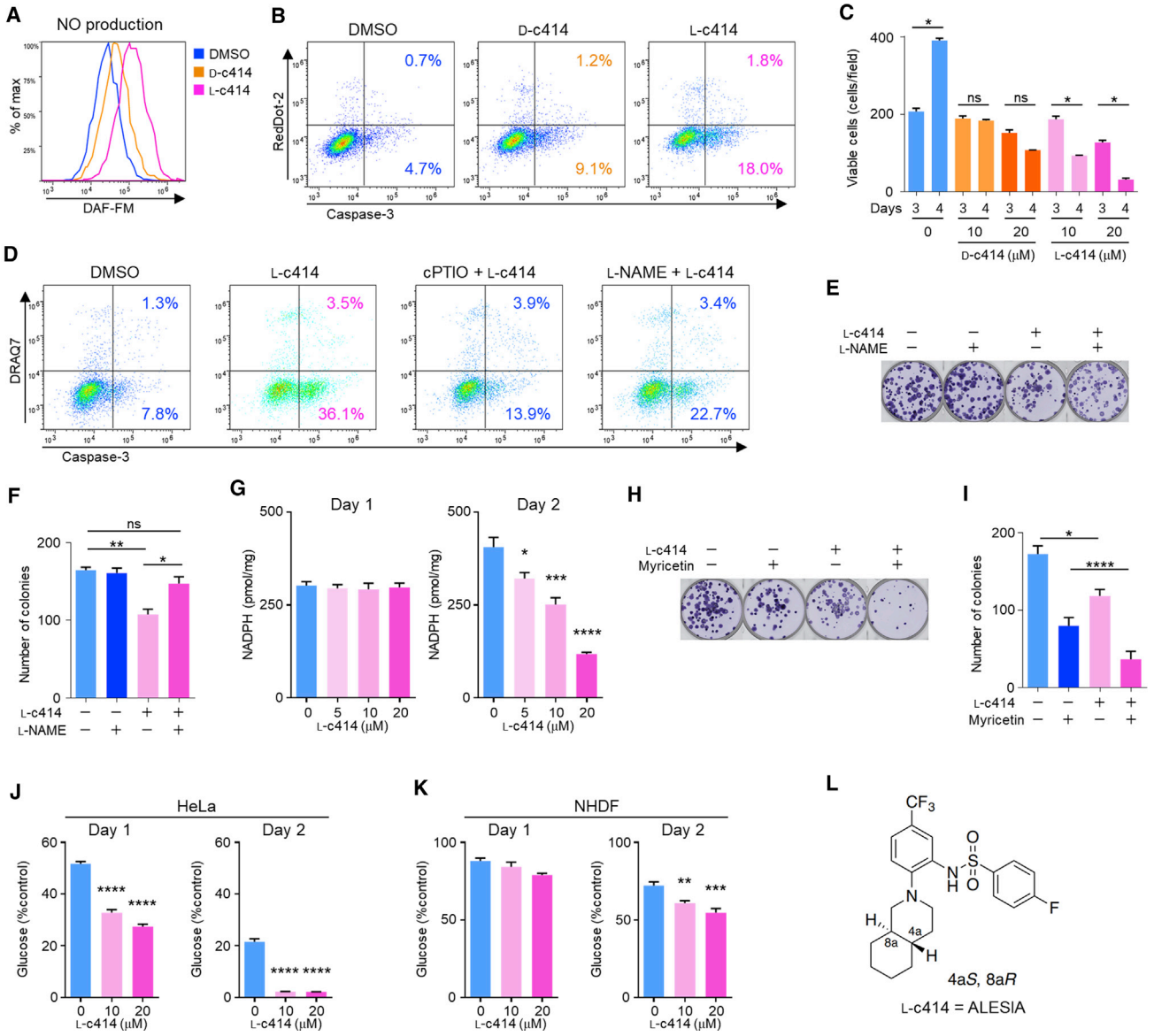

Figure 2. ALESIA causes both glucose starvation and cell death in cancer cells by inducing NO production

(A and B) NO production (A) and apoptosis (B) in HeLa cells treated with 20 μM D-c414 or L-c414 for 3 days. The cells were stained with an active caspase-3 indicator NucView488 and the dead cell indicator RedDot-2.

(C) HeLa cells were treated with D-c414 or L-c414 for 3 or 4 days, respectively. Cells were analyzed using calcein staining. Error bars, SEM (n = 3).

(D) Apoptosis of HeLa cells treated with 10 μM L-c414 for 15 h in a glucose-free medium. The cells were stained with NucView488 and the dead cell indicator DRAQ7. HeLa cells were incubated with the vehicle, cPTIO (0.2 mM), or N^G-nitro-L-arginine methyl ester (L-NAME; 4 mM) for 1 h before L-c414 was added.

(E and F) Representative images (E) and quantification of colony numbers (F) of clonogenic cell survival assay for HeLa cells. The cells were fixed with methanol and stained with crystal violet. HeLa cells were treated with L-c414 (10 μM) and L-NAME (1 mM) for 14 days. Error bars, SEM (n = 3).

(G) NADPH concentration in HeLa cells after L-c414 treatment. Error bars, SEM (n = 4).

(H and I) Representative images (H) and quantification of colony numbers (I) of clonogenic cell survival assay for HeLa cells. HeLa cells were treated with L-c414 (10 μM) and myricetin (6 μM) for 14 days. Error bars, SEM (n = 4).

(J and K) Residual glucose levels in the culture medium of HeLa cells (J) or NHDFs (K) after L-c414 treatment. Error bars, SEM (n = 6).

(L) Chemical structure of ALESIA. In (C), (F), and (I), *p < 0.05, **p < 0.01, ****p < 0.0001 (Tukey's test).

In (G), (J), and (K), *p < 0.05, **p < 0.01, ***p < 0.001, ****p < 0.0001 (Tukey's test, compared with DMSO control); ns, not significant.

We have confirmed that ALESIA increases glucose consumption and leads to glucose depletion in cancer cells (Figure 2J), and that low-glucose conditions induce NADPH deficiency (Figure 2G) and enhance its anticancer effects (Figures 3E–3H). Similarly, to confirm that the suppression of NADPH production enhanced the effects of ALESIA, we also examined cell proliferation after hexokinase inhibition. Here, we examined using cervical cancer C33A cells suitable for xenograft experiments. As expected, the combined use of the hexokinase inhibitor 2DG and ALESIA markedly suppressed C33A cell proliferation

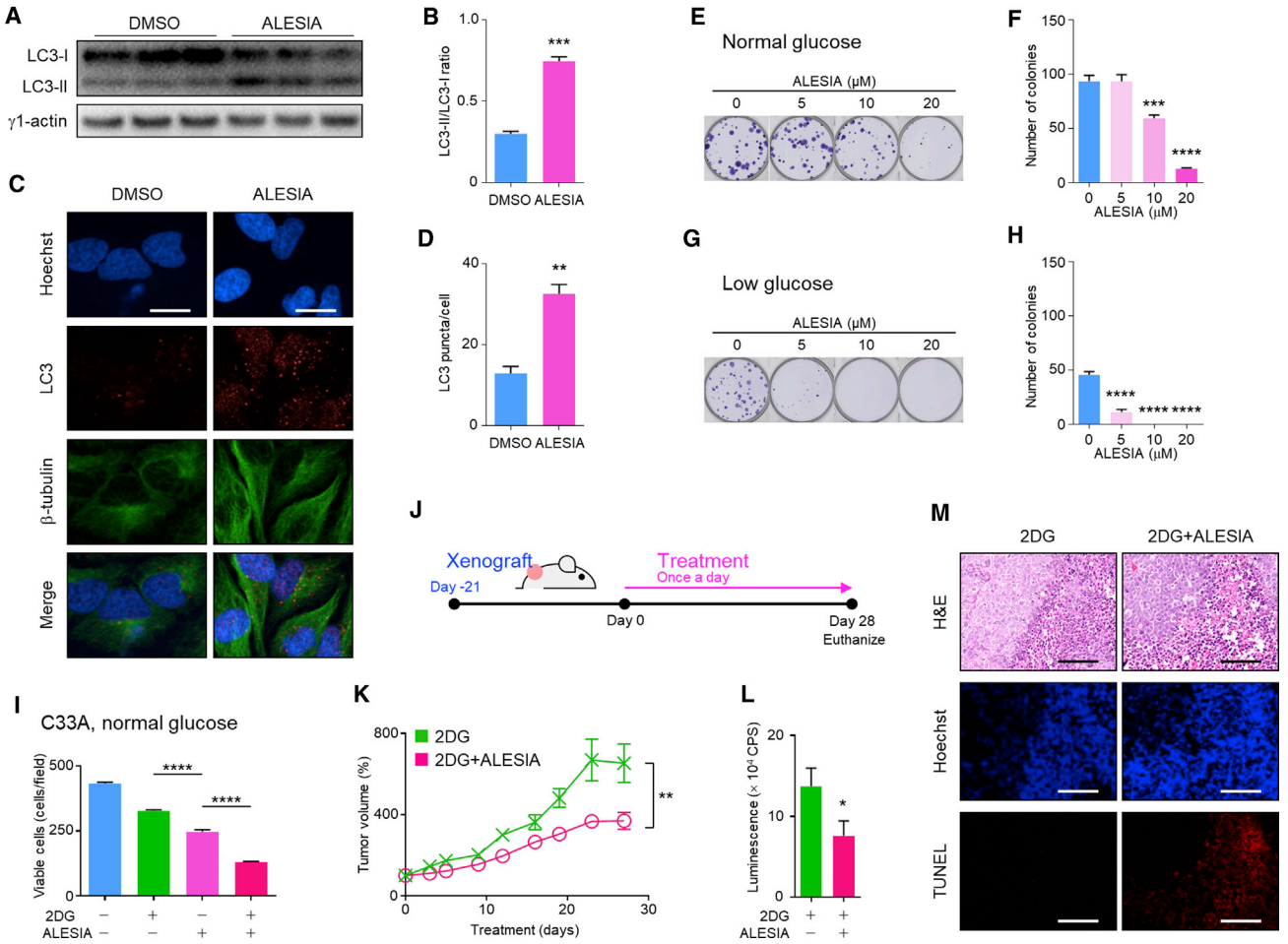

Figure 3. Suppression of NADPH production enhances the effects of ALESIA

(A and B) Immunoblot analysis of microtubule-associated protein 1A/1B-light chain 3 (LC3) and γ1-actin in HeLa cells. Immunoblot images (A) and densitometric analysis of LC3-II/LC3-I ratio (B). HeLa cells were treated with 20 μM ALESIA for 2 days. Error bars, SEM (n = 3). ***p < 0.001 (Student's t test). The images are representative of two experiments.

(C and D) Immunofluorescent analysis of LC3 in HeLa cells. Confocal microscopic images (C) and the numbers of LC3 puncta per cell (D). HeLa cells were treated with 10 μM ALESIA for 2 days and visualized by using Opera after LC3, β-tubulin, and Hoechst 33342 staining. The numbers of LC3 puncta per cell were calculated by using Opera. Scale bars correspond to 20 μm. Error bars, SEM (n = 3). **p < 0.01 (Student's t test).

(E–H) Clonogenic cell survival assay for ALESIA in HeLa cells. The cells were fixed with methanol and stained with crystal violet. HeLa cells were treated with ALESIA for 14 days under normal-glucose (E and F) and low-glucose (G and H) conditions. Error bars, SEM (n = 4). ***p < 0.001, ****p < 0.0001 (Tukey's test, compared with DMSO control).

(I) C33A cells were treated with 22DG (2 mM), ALESIA (10 μM), or 2DG with ALESIA for 1 day and analyzed using calcein staining. Error bars, SEM (n = 4). ****p < 0.0001 (Tukey's test).

(J) Schematic of the xenografted mouse experiments.

(K) Subcutaneous growth of C33A cells producing GLuc in mice. Mice (BALB/c-nu/nu) were inoculated with C33A cells and treated with the 2DG or 2DG with ALESIA orally. Error bars, SEM (n = 9). **p < 0.01 (two-way ANOVA).

(L) GLuc activity in the serum 28 days after treatment. Error bars, SEM (n = 9). *p < 0.05 (Student's t test).

(M) End-stage tumor sections from 2DG- or 2DG with ALESIA-treated mice, stained with hematoxylin and eosin (H&E), or Hoechst 33342, and subjected to TUNEL assay. Scale bars, 100 μm.

in vitro (Figure 3I) and *in vivo* (Figures 3J–3M), whereas the treatment had no adverse effect on the weight of xenograft mice (Figure S3).

ALESIA binds to sphingosine-1-phosphate receptor 3

In the regulation of TXNIP expression by glucose, AMP-activated protein kinase (AMPK) plays a crucial role (Wu et al., 2013). The decrease in TXNIP abundance induced by ALESIA treatment suggests that ALESIA contributes to AMPK activation. In addition, we sought to identify the putative targets of ALESIA by searching the SciFinder database for structural similarities between ALESIA and other compounds with known targets/signaling pathways. The search results also suggested that ALESIA could be an AMPK activator. We administered ALESIA to murine bone marrow-derived macrophages (BMMs) to examine whether ALESIA activated the AMPK pathway since BMMs

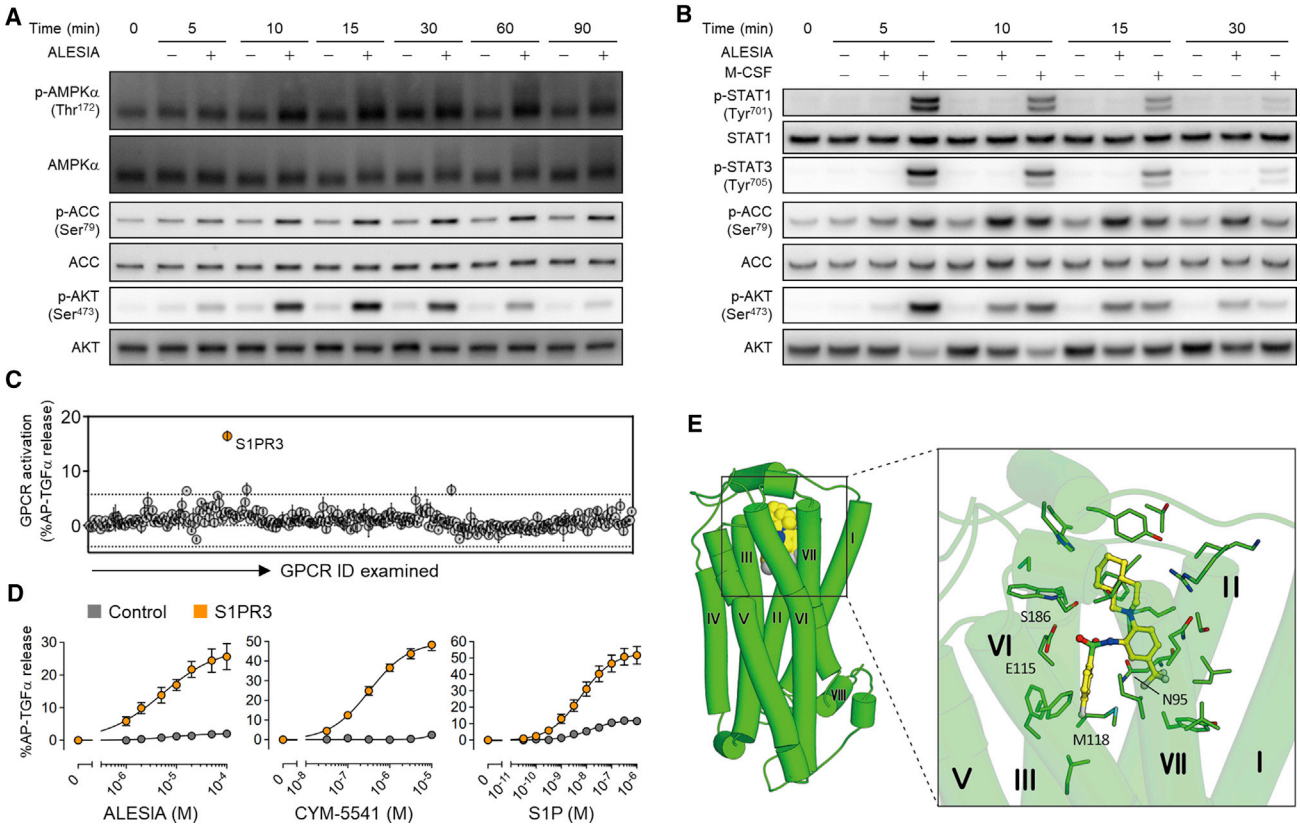

Figure 4. ALESIA is an S1PR3 agonist

(A) Immunoblot analysis of phosphorylated AMPK, ACC, and AKT in murine BMMs treated with ALESIA after an 8-h starvation with M-CSF.

(B) Immunoblot analysis of phosphorylated signal transducer and activator of transcription (STAT) 1, STAT3, AKT, and ACC. BMMs were treated with DMSO, ALESIA (50 μM), or M-CSF (50 ng/mL) after an 8-h M-CSF starvation.

(C) GPCR screening using TGFα shedding assay.

(D) Activation of S1PR3 by ALESIA, a selective agonist, or a natural ligand using TGFα shedding assays. Error bars, SEM (n = 4).

(E) Docked structure for ALESIA (model 1), viewed from the membrane plane. S1PR3 and ALESIA are shown as green cylinders and yellow Corey-Pauling-Koltun (CPK) model, respectively. Right panel, zoomed in the ALESIA-binding site. ALESIA and contact residues are shown as sticks colored in yellow and green, respectively.

express the macrophage colony-stimulating factor (M-CSF) receptor and are sensitive to M-CSF. The result shows that ALESIA treatment enhanced the phosphorylation of AMPK and acetyl coenzyme A (CoA) carboxylase (ACC, an AMPK substrate) in both HeLa cells and BMMs (Figure S4A and 4A), although an *in vitro* kinase assay revealed that ALESIA indirectly activated AMPK (Figure S4B). Moreover, ALESIA induced the phosphorylation of AKT within 5 min (Figure 4A). Hence, we hypothesized that the cellular target of ALESIA is a cell-surface receptor. Receptors capable of simultaneously phosphorylating both AMPK and AKT were considered to be either G protein-coupled receptors (GPCRs) or receptor tyrosine kinases (Lappano and Maggiolini, 2011). If ALESIA activates the receptor tyrosine kinase pathway, tyrosine phosphorylation of the signal transducer and activator of transcription (STAT) 1 or STAT3 would be induced (Lappano and Maggiolini, 2011). However, ALESIA failed to enhance tyrosine phosphorylation in BMMs, whereas M-CSF, a positive control, induced the phosphorylation of both (Figure 4B). Thus, we reasoned that the target molecule of ALESIA must be a GPCR and assessed the activation of 226 types of mainly class A GPCRs (Hauser et al., 2017) induced by ALESIA using the transforming growth factor α (TGFα) shedding assay in HEK293A cells (Inoue et al., 2012). In this assay, GPCR activation is determined based on the ectodomain shedding of alkaline phosphatase-tagged TGFα (AP-TGFα) (Inoue et al., 2012). ALESIA induced the shedding of AP-TGFα only in sphingosine-1-phosphate receptor 3 (S1PR3)-expressing cells (Figure 4C) in a concentration-dependent manner with the negative logarithm of the half maximal effective concentration (pEC_{50}) = 5.34 ± 0.15 (Figures 4D and S5A). Docking simulations with S1PR3 agonists (Figure S5B) indicated that ALESIA binds to the putative orthosteric binding site of S1PR3 (Figure 4E). Furthermore, the inhibitory effect of ALESIA on HeLa cell proliferation was significantly diminished by the S1PR3 antagonist CAY10444 (Figure S6A). The selective agonist of S1PR3, CYM-5541 (Jo et al., 2012), and the endogenous ligand sphingosine-1-phosphate (S1P) also stimulated the release of AP-TGFα in a concentration-dependent manner, with pEC_{50} values of 6.49 ± 0.11 and 8.22 ± 0.06, respectively (Figures 4D and S5A). S1P inhibits the Hippo pathway kinases, large tumor suppressor kinase 1/2 (LATS 1/2) through $G_{12/13}$-coupled receptors. Inhibition of LATS 1/2 activates Yes-associated protein (YAP) transcription

coactivator by dephosphorylation of YAP (Yu et al., 2012). Therefore, we analyzed the effect of ALESIA on YAP phosphorylation state in HeLa cells using immunoblot and found that ALESIA enhanced dephosphorylation of YAP, although the effect is much weaker than that of S1P (Figures S6B and S6C).

ALESIA is a biased agonist of S1PR3 and specifically transmits the signal to G_{12}

Rhabdomyosarcoma A-204 cells express high levels of S1PR3 (Ghandi et al., 2019) and were most sensitive to ALESIA in the cancer panel under normal-glucose conditions (Table S1). Therefore, we tested the NO production ability of each S1PR3 agonist in A-204 cells. ALESIA induced NO synthesis more significantly than CYM-5541 (Figure S6D), although the pEC_{50} value of ALESIA was lower than that of CYM-5541. Unlike the tumor growth-inhibiting effect of ALESIA (Figures S6E and S6F), it is reported that both S1P and CYM-5541 have tumor growth-promoting effects provably through prostaglandin E2 production (Filipenko et al., 2016; Kunkel et al., 2013; Visentin et al., 2006; Wang and Dubois, 2010; Yu et al., 2018). Based on these findings, we hypothesized that ALESIA is of a different type of S1PR3 agonist from CYM-5541.

S1PR3 transmits the S1P-induced signals via G_i, $G_{q/11}$, and $G_{12/13}$ (Inoue et al., 2019; Windh et al., 1999). Among these, G_{12} is reported to enhance the total endothelial NOS (eNOS) activity (Andreeva et al., 2006). To analyze the ALESIA-induced signal transduction downstream of S1PR3, we evaluated the activation of TGFα shedding in cells where either the G_q or G_{12} gene was deleted. As expected, ALESIA did not induce shedding activity in G_{12}-deficient HEK293A cells, whereas CYM-5541 and S1P did (Figure 5A and S6G). In addition, in G_{12}-deficient HEK293A cells, ALESIA failed to induce NO production via S1PR3 (Figure 5B).

Next, we evaluated the recruitment of β-arrestin to S1PR3 by the agonists. The involvement of β-arrestin in GPCR desensitization is controlled by *S*-nitrosylation attributed to NO (Whalen et al., 2007). The cellular trafficking of β-arrestin was evaluated using the NanoLuc Binary Technology (NanoBiT). In this assay, the recruitment of β-arrestin to the plasma membrane after agonist stimulation of S1PR3 in HEK293A cells was monitored based on the luminescence signal between SmBiT–S1PR3 fusion and LgBiT–β-arrestin fusion proteins. S1P and CYM-5541 caused a significant increase in luminescence, whereas ALESIA did not, having neither β-arrestin1 nor β-arrestin2 (Figures 5C and S6H). These experiments collectively support a model in which ALESIA stimulates S1PR3–G_{12} biasedly, as shown in Figure 6.

ALESIA improves survival against rhabdomyosarcoma expressing high levels of S1PR3

To evaluate its applicability to cancer starvation therapy, we tested its effect on A-204 cells both *in vitro* and *in vivo*. As expected, ALESIA dramatically reduced the clonogenic survival of A-204 cells in a dose-dependent manner (Figures 7A and 7B). Before the *in vivo* experiment, we confirmed the safety of ALESIA administration. BALB/c mice were intraperitoneally administered with a 50-mg/kg/dose of ALESIA 10 times for 2 weeks. As the administration showed no adverse effects in mice (Figure S7A), we proceeded to its *in vivo* testing. Severe combined immunodeficient (SCID) mice were intraperitoneally implanted with A-204 cells (5×10^6 cells per mouse), which stably express *Gaussia* luciferase (GLuc) as a marker (Figure 7C). Seven weeks after the implantation, we divided them into two groups after normalizing the average GLuc activity in the blood (Figure S7B). Subsequently, we intraperitoneally administered a 50-mg/kg/dose of ALESIA to these mice 40 times for 8 weeks. ALESIA administration significantly improved the survival in mice with the A-204 xenograft ($p < 0.05$; Figure 7D).

DISCUSSION

In this study, we identified a unique S1PR3–G_{12}-biased agonist from a phenotypic screening and named it ALESIA. ALESIA promoted NO production and oxidative stress in the treated cells. In order to reduce this oxidative stress, cancer cells need to produce more NADPH. Generation of NADPH leads to further glucose depletion in cancer cells, while normal cells are able to cope. Eventual glucose exhaustion impaired cancer cell defense against oxidative stress, yielding apoptosis selectively in cancer cells. Consequently, ALESIA selectively induced cell death in the tumor, without any adverse effects on healthy tissues even *in vivo*.

It had been generally believed that AKT is involved in controlling energy metabolism, which is coupled to its ability to inhibit apoptosis induced by a variety of apoptotic stimuli and to promote cell-cycle progression in mammalian cells (Plas and Thompson, 2005). However, Nogueira et al. (2008) reported that cancer cells expressing activated AKT are selectively killed by oxidative stress. Our observation that the administration of ALESIA induced AKT phosphorylation and enhanced apoptosis in HeLa cells is consistent with that of Nogueira et al. (2008). ALESIA induces oxidative stress via the S1PR3–G_{12}-mediated NO production and selectively promotes apoptosis in cancer cells, which cannot produce sufficient NADPH through the pentose-phosphate pathway because of glucose exhaustion. In fact, the normal cells treated with ALESIA *in vitro* were not adversely affected, and the mice intraperitoneally administrated with ALESIA gained weight normally without showing any toxic symptoms after observation for 2 weeks. ALESIA did not give any toxic effect in normal proliferating cells, such as intestinal epithelial cells and bone marrow cells, which are susceptible to chemotherapy and radiotherapy, because they can still regulate mitochondrial oxidative phosphorylation (Zheng, 2012). However, we cannot deny the possibility that ALESIA gives an adverse effect in other immune cells and stem cells that reprogram their metabolism in a manner similar to cancer (Ito and Suda, 2014; Pearce et al., 2013). S1PR3 is known to be expressed in many types of normal cells. In the case of human immune cells, S1PR3 expression is confirmed in B lymphocytes, monocytes, macrophages, neutrophils, eosinophils, mast cells, and dendritic cells (Blaho and Hla, 2014), and is reported to be required for normal B cell development (Donovan et al., 2010). Rodent heart has abundant expression of S1PR3 on myocytes and perivascular smooth muscle cells (Forrest et al., 2004; Sanna et al., 2004). Although the effect of ALESIA on normal cells was limited (for example, 20% inhibitory concentration of ALESIA on splenocyte proliferation was over 10 μM in 3-day culture), the development of ALESIA and its derivatives for their practical uses as anticancer agents with

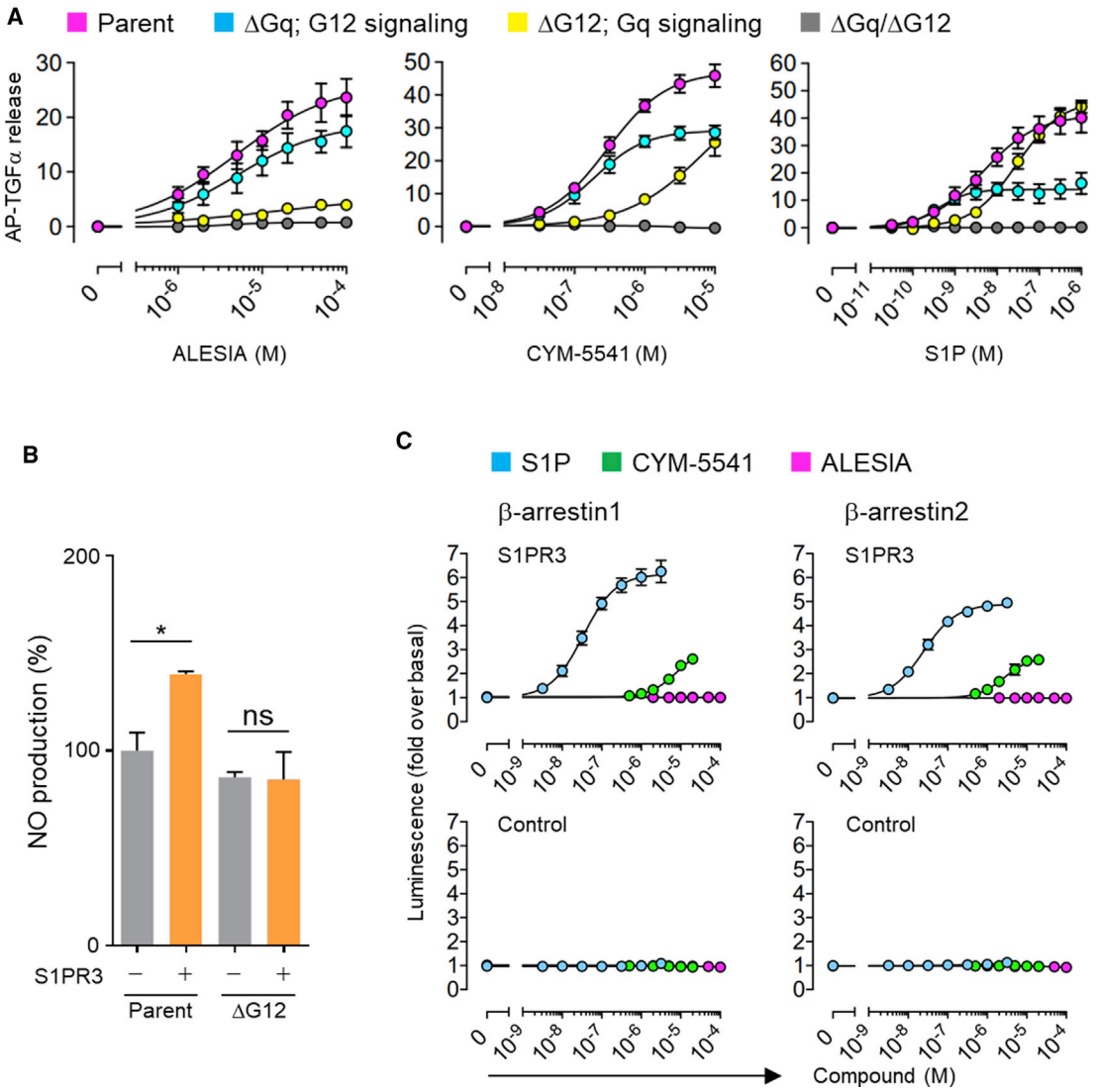

Figure 5. ALESIA exhibits an original G_{12}-biased agonism

(A) Activation of S1PR3 by ALESIA, a selective agonist, or by a natural ligand induces TGFα shedding via both G_q and G_{12}. ΔGq, cells lacking G_q; ΔG12, cells lacking G_{12}; ΔGq/ΔG12, cells lacking both G_q and G_{12}. Error bars, SEM (n = 3–4).

(B) NO production induced by ALESIA. HEK293A cells were transfected with the control vector or the S1PR3 expression vector. After 2 days, they were treated with 10 μM ALESIA for 18 h in DMEM containing 0.2 g/L glucose and 1% FBS and stained with DAF-FM. Error bars, SEM (n = 3). *$p < 0.05$ (Tukey's test).

(C) Dose-response curves for NanoBiT–β-arrestin recruitment to S1PR3 by agonists. HEK293A parental cells were transiently transfected with *S1PR3* and assayed the following day. Error bars, SEM (n = 4–6).

caution for the potency of adverse effects on these cells is crucial.

The assessment of the activation of 226 GPCRs through the TGFα shedding assay suggested that ALESIA was a specific agonist of S1PR3, although ALESIA weakly activated bradykinin receptor B1, adenosine A1 receptor, G Protein-Coupled Receptor 17, and lysophosphatidic acid receptor 5 at the low-μM range. Rhabdomyosarcoma is a typical childhood tumor, but adult-onset rhabdomyosarcoma often has a worse outcome (Sultan et al., 2009). The rhabdomyosarcoma cell line A-204 highly expresses S1PR3 mRNA (Ghandi et al., 2019) and was the most vulnerable to ALESIA in our cancer panel analysis. Therefore, we used A-204 xenograft mice for the *in vivo* test, and ALESIA significantly improved their survival, as expected. However, our analysis of RNA-seq data for cancer cells indicated that the expression levels of S1PR3 do not simply determine the sensitivity of cancer cells to ALESIA and suggested the possibility that fatty acid metabolism may affect it. In order to find out the best target of ALESIA for clinical application, we need to further analyze the cellular factors that cause the anticancer effect.

Several studies have addressed that the binding of S1P to S1PR3 suppresses the activation of autophagy (Ghosal et al., 2016; Taniguchi et al., 2012), whereas ALESIA induced

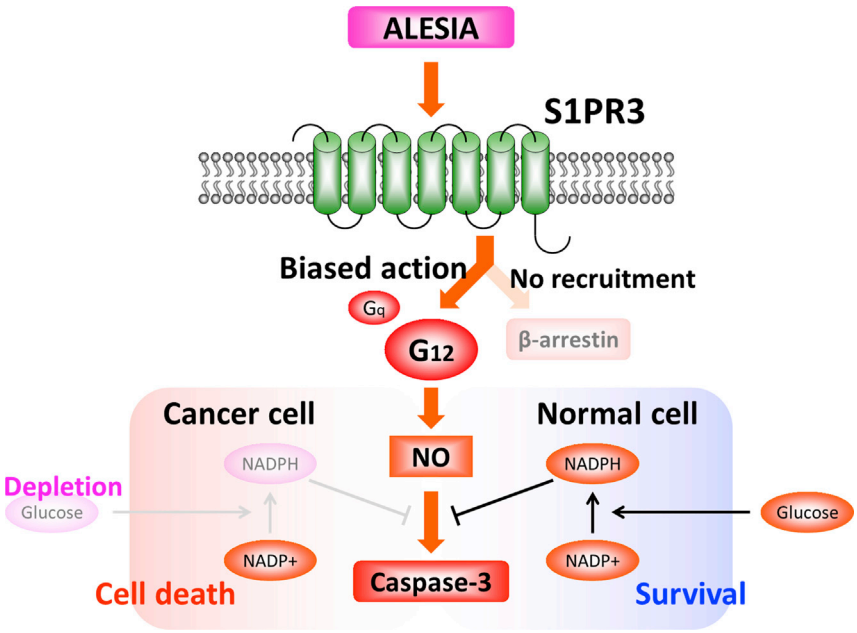

Figure 6. Schematic overview of the proposed action mechanism of ALESIA

ALESIA strongly promotes NO production via the S1PR3–G_{12}-biased action without β-arrestin recruitment. The cells then consume cellular NADPH to reduce the oxidative stress caused by increased levels of NO. Because cancer cells store considerably less glucose compared with normal cells, NADPH generation from $NADP^+$ leads to the depletion of cellular glucose in cancer cells, but normal cells are tolerant because they stock enough. Glucose exhaustion in cancer cells results in the lack of cellular defenses owing to NADPH deficiency, and excess oxidative stress eventually induces their cell death, whereas normal cells survive.

autophagy. This discrepancy could be explained by the distinctive feature of ALESIA, which functions as an S1PR3–G_{12}-biased agonist because G_{12} overexpression induces the activation of autophagy (Kim et al., 2018). Chemotherapy drugs, such as doxorubicin, paclitaxel, and docetaxel, are also autophagy inducers (Ramakrishnan et al., 2012) and provoke oxidative stress (Pieniazek et al., 2013). Thus, the combining existing anticancer drugs with ALESIA may positively enhance their therapeutic effects on cancer. In addition, ALESIA may improve the efficacy of chemo-radiotherapy as the glycolytic inhibitor 2DG improved chemo-radio-sensitization in a clonogenic survival assay (Coleman et al., 2008; Lin et al., 2003). Although the MAPK14/p38α-dependent modulation of glucose metabolism affects ROS levels and autophagy during starvation (Desideri et al., 2014), we could not detect significant ROS production using ALESIA treatment, suggesting that the S1PR3–G_{12}-biased agonistic pathway is independent of the MAPK14/p38α signal. It has been reported that activation of AKT and AMPK phosphorylates and activates eNOS enzyme, thereby leading to NO production (Fulton et al., 1999; Gupta et al., 2017). However, further studies are needed regarding the involvement of AKT and AMPK in NO production via S1PR3–G_{12}.

S1P has been implicated in cancer progression by regulating tumor proliferation and invasion through inhibition of the Hippo pathway with YAP dephosphorylation (Yu et al., 2018). ALESIA also induced YAP dephosphorylation, but the effect was much weaker than that of S1P, suggesting the possibility that we can develop more potent anticancer derivatives of ALESIA if the inhibitory effect on LATS 1/2 is minimized. ALESIA selectively transmits the G_{12}-protein signal without the recruitment of β-arrestin to the plasma membrane upon S1PR3 action and induces the excessive production of NO. Thus, ALESIA is a unique biased agonist of S1PR3 (Violin et al., 2014), the structure of which remains unknown. Drug discovery based on the concept of biased agonism yields new therapeutics, the usage of which is devoid of the adverse effects of existing drugs (Bologna et al., 2017; Galvani et al., 2015; Kenakin and Christopoulos, 2013; Manglik et al., 2016). For example, an opioid agonist, which has G protein-biased modulation, can eliminate adverse effects such as the respiratory depression mediated by β-arrestin signaling (DeWire et al., 2013; Manglik et al., 2016). Therefore, we intend to elucidate the crystal structure of the S1PR3/ALESIA complex to reveal its G_{12}-biased signaling mechanism. This information would allow the development of a new type of biased agonists of GPCRs and remarkably expand the field of drug discovery.

SIGNIFICANCE

Our results indicated that ALESIA is a unique biased agonist of S1PR3, which supported the finding that ALESIA strongly induced NO production and selectively killed cancer cells. Its elucidated mode of action is as follows: (1) ALESIA promotes NO production by stimulating S1PR3–G_{12} coupling without β-arrestin recruitment; (2) cancer cells consume NADPH to reduce the oxidative stress associated with induced NO production, thereby requiring more glucose than usual for NADPH supplementation; (3) the eventual depletion of glucose leads to NADPH deficiency and impairs cellular defenses against oxidative stress; and (4) the oxidative stress eventually kills cancer cells, whereas normal cells can survive because of greater glucose storage. In tumor model experiments, ALESIA administration improves survival in xenograft mice of rhabdomyosarcoma expressing high levels of S1PR3. These findings support the hypothesis that ALESIA is a new type of biased agonist targeting S1PR3 and could be used for an anticancer drug that enhances the effects of glucose starvation therapy. Additionally, the discovery of ALESIA provides the tool to elucidate the physiological role of the S1PR3-biased signaling, giving us insights into the presence of an endogenous biased ligand that modulates signaling in four major families of heterotrimeric G protein.

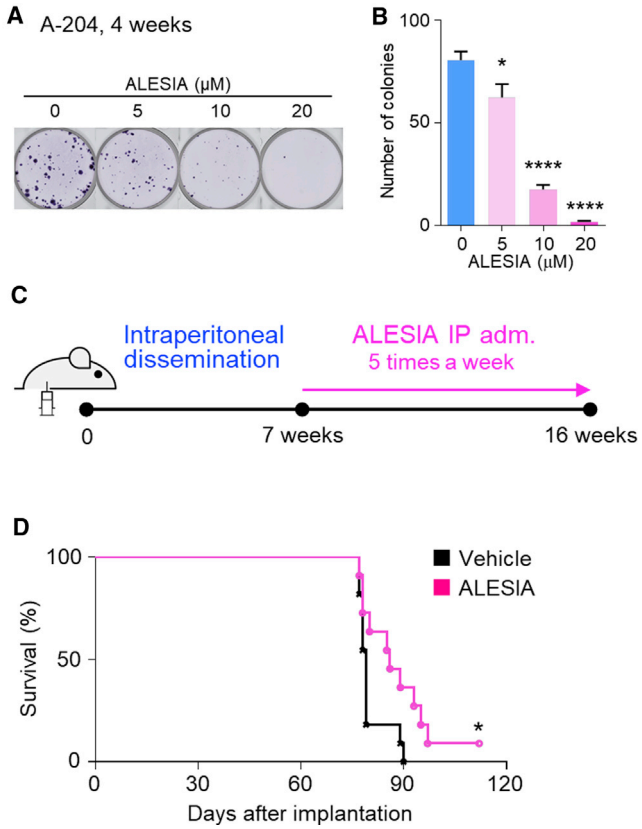

Figure 7. ALESIA attenuates death in a xenograft model with peritoneal dissemination of rhabdomyosarcoma

(A and B) Representative images (A) and quantification of colony numbers (B) of clonogenic cell survival assay for A-204 cells. A-204 cells were treated with ALESIA for 4 weeks. The cells were fixed with methanol and stained with crystal violet. Error bars, SEM (n = 4). *p < 0.05, ****p < 0.0001 (Tukey's test, compared with DMSO control).

(C) Schematic of the xenografted mouse experiments.

(D) The survival rate in xenografted mice treated with a vehicle (saline with 0.05% Tween 80) or ALESIA (50 mg/kg; n = 11 mice per group). *p < 0.05 (Log rank test).

STAR★METHODS

Detailed methods are provided in the online version of this paper and include the following:

- KEY RESOURCES TABLE
- RESOURCE AVAILABILITY
  - Lead contact
  - Materials availability
  - Data and code availability
- EXPERIMENTAL MODEL AND SUBJECT DETAILS
  - Animals
  - Cell lines
  - Primary cultures
  - Preparation of Gaussia luciferase (GLuc)-stable C33A cells for xenograft tumor formation
  - Xenograft model
  - Preparation of GLuc-stable A-204 cells for intraperitoneal dissemination xenograft model
  - Xenograft model with intraperitoneal dissemination
- METHOD DETAILS
  - Plasmid construction
  - In *vitro* phenotypic screening
  - Cell proliferation and cytotoxicity assay
  - Cell viability assays
  - Apoptotic cell analysis
  - RNA-sequencing (RNA-seq) experiment and data analysis
  - QuantitativeRT-PCR (RT-qPCR)
  - Immunoblotting
  - Determination of intracellular nitric oxide
  - Determination of intracellular reactive oxygen species
  - Determination of caspase-3 activity
  - In *vitro* kinase assay
  - TGFα shedding assay
  - NanoBiT–β-arrestin recruitment assay
  - NADPH measurements
  - Glucose assay
  - Clonogenic cell survival assay
  - Immunofluorescent analysis
  - Histology and TUNEL staining
  - GLuc serum assay
  - GLuc assay
  - Cancer panel
  - Data analysis of the cancer panel
  - Model prediction and docking simulation
  - Pathway analysis
- QUANTIFICATION AND STATISTICAL ANALYSIS

SUPPLEMENTAL INFORMATION

Supplemental information can be found online at https://doi.org/10.1016/j.chembiol.2021.01.004.

ACKNOWLEDGMENTS

We thank A. Kobayashi, M. Ajiro, M. Yamamoto, S. Ohmae, Y. Sako, E. Kanemitsu, T. Motoki, K. Motomura, T. Sawada, K. Hayashi, Y. Okuno, S. Shibata, and the M.H. laboratory members for their helpful contributions to discussions and technical assistance; K. Tomooka and K. Igawa (Kyushu University) for their help in X-ray crystal structure analysis; the Medical Research Support Center, Graduate School of Medicine, Kyoto University, for compound screening; and the Institute of Laboratory Animals and the Center for Anatomical, Pathological, and Forensic Medical Research, Graduate School of Medicine, Kyoto University, for microscopy slide preparations. We would also like to thank Editage (www.editage.jp) for English language editing.

Funding: this work was supported by grants-in-aid from the Japan Agency for Medical Research and Development (AMED; grant numbers JP16lk0103007h0005, JP16bk0104034h0003, JP161m0103006j0005(c-6-2), JP18kk0305003h0003, JP18am0101092, JP18bm0804007h0002, and 19ek0109310h0002 to T.H. and M.H.; JP18gm5910013 to A.I.; JP18gm0010004 to A.I. and J.A.), AMED-CREST (Create Revolutionary Technological Seeds for Science and Technology Innovation; grant number JP16gm0510008h0006 to T.H. and M.H.), AMED-BINDS (Basis for Supporting Innovative Drug Discovery and Life Science Research; grant number JP19am0101092 to M.H. and T.H.; JP20am0101079 to S.I.), the Japanese Ministry of Education, Culture, Sports, Science, and Technology (MEXT; grant number 15H05721 to T.H. and M.H.), the Ministry of Health, Labour and Welfare of Japan (to M.H.), PRESTO from Japan Science and Technology Agency (JST; grant number JPMJPR1331 to A.I.), and Japan Society for the Promotion of Science (JSPS) KAKENHI (grant number JP19H05777 to S.I.).

AUTHOR CONTRIBUTIONS

M.T. performed most of the cell biological experiments, *in vivo* studies, and analyses. M.T. and M.H. designed the project, analyzed the data, interpreted the results, and compiled the original draft of the manuscript with inputs from all authors. A.I., F.M.N.K., and T.K. performed the TGFα shedding and the NanoBiT–β-arrestin recruitment assays and analyzed the data. K.I. and M.D. performed RNA-seq and analyzed the RNA-seq data. I.K. and H.O. performed the initial experiments to identify the anticancer effects of tested compounds. D.I. performed the ligand-docking simulations. S.Y. performed the chemical syntheses, separation, and identification of compounds. T.S., S.I., J.A., and T.H. supervised and mentored other co-authors and interpreted the experimental data. All authors participated in the preparation of the manuscript.

DECLARATION OF INTERESTS

M.T., I.K., S.Y., T.H., and M.H. filed patent PCT/JP2016/063381 for ALESIA. M.T., S.Y., T.H., and M.H. filed patent PCT/JP2017/039426 for ALESIA. H.O. is a chief operating officer of KinoPharma, Inc. M.H. is a founder, shareholder, and member of the scientific advisory board of KinoPharma, Inc., and BTB Drug Development Research Center Co., Ltd, although both companies are not directly involved in ALESIA. The other authors declare that they have no competing interests.

Received: May 18, 2020
Revised: December 7, 2020
Accepted: January 6, 2021
Published: February 8, 2021

REFERENCES

Ajiro, M., Sakai, H., Onogi, H., Yamamoto, M., Sumi, E., Sawada, T., Nomura, T., Kabashima, K., Hosoya, T., and Hagiwara, M. (2018). CDK9 inhibitor FIT-039 suppresses viral oncogenes E6 and E7 and has a therapeutic effect on HPV-induced neoplasia. Clin. Cancer Res. *24*, 4518–4528.

Alderton, W.K., Cooper, C.E., and Knowles, R.G. (2001). Nitric oxide synthases: structure, function and inhibition. Biochem. J. *357*, 593–615.

Andreeva, A.V., Vaiskunaite, R., Kutuzov, M.A., Profirovic, J., Skidgel, R.A., and Voyno-Yasenetskaya, T. (2006). Novel mechanisms of g protein-dependent regulation of endothelial nitric-oxide synthase. Mol. Pharmacol. *69*, 975–982.

Bao, W., Kojima, K.K., and Kohany, O. (2015). Repbase Update, a database of repetitive elements in eukaryotic genomes. Mob. DNA *6*, 11.

Benhar, M., Forrester, M.T., and Stamler, J.S. (2009). Protein denitrosylation: Enzymatic mechanisms and cellular functions. Nat. Rev. Mol. Cell Biol. *10*, 721–732.

Berruti, A., Bitossi, R., Gorzegno, G., Bottini, A., Alquati, P., De Matteis, A., Nuzzo, F., Giardina, G., Danese, S., De Lena, M., et al. (2002). Time to progression in metastatic breast cancer patients treated with epirubicin is not improved by the addition of either cisplatin or lonidamine: final results of a phase III study with a factorial design. J. Clin. Oncol. *20*, 4150–4159.

Blaho, V.A., and Hla, T. (2014). Thematic review series: lysophospholipids and their receptors: an update on the biology of sphingosine 1-phosphate receptors. J. Lipid Res. *55*, 1596–1608.

Bologna, Z., Teoh, J., Bayoumi, A.S., Tang, Y., and Kim, I. (2017). Biased G protein-coupled receptor signaling: new player in modulating physiology and pathology. Biomol. Ther. (Seoul) *25*, 12–25.

Cao, X.M., Luo, X.G., Liang, J.H., Zhang, C., Meng, X.P., and Guo, D.W. (2012). Critical selection of internal control genes for quantitative real-time RT-PCR studies in lipopolysaccharide-stimulated human THP-1 and K562 cells. Biochem. Biophys. Res. Commun. *427*, 366–372.

Coleman, M.C., Asbury, C.R., Daniels, D., Du, J., Aykin-Burns, N., Smith, B.J., Li, L., Spitz, D.R., and Cullen, J.J. (2008). 2-Deoxy-d-glucose causes cytotoxicity, oxidative stress, and radiosensitization in pancreatic cancer. Free Radic. Biol. Med. *44*, 322–331.

DeBerardinis, R.J., and Chandel, N.S. (2016). Fundamentals of cancer metabolism. Sci. Adv. *2*, e1600200.

Desideri, E., Vegliante, R., Cardaci, S., Nepravishta, R., Paci, M., and Ciriolo, M.R. (2014). MAPK14/p38α-dependent modulation of glucose metabolism affects ROS levels and autophagy during starvation. Autophagy *10*, 1652–1665.

Devost, D., Sleno, R., Pé Trin, D., Zhang, A., Shinjo, Y., Okde, R., Aoki, J., Inoue, A., and Hébert, T.E. (2017). Conformational profiling of the AT1 angiotensin II receptor reflects biased agonism, G protein coupling, and cellular context. J. Biol. Chem. *292*, 5443–5456.

DeWire, S.M., Yamashita, D.S., Rominger, D.H., Liu, G., Cowan, C.L., Graczyk, T.M., Chen, X.-T., Pitis, P.M., Gotchev, D., Yuan, C., et al. (2013). A G protein-biased ligand at the μ-opioid receptor is potently analgesic with reduced gastrointestinal and respiratory dysfunction compared with morphine. J. Pharmacol. Exp. Ther. *344*, 708–717.

Dixon, A.S., Schwinn, M.K., Hall, M.P., Zimmerman, K., Otto, P., Lubben, T.H., Butler, B.L., Binkowski, B.F., MacHleidt, T., Kirkland, T.A., et al. (2016). NanoLuc complementation reporter optimized for accurate measurement of protein interactions in cells. ACS Chem. Biol. *11*, 400–408.

Dobin, A., Davis, C.A., Schlesinger, F., Drenkow, J., Zaleski, C., Jha, S., Batut, P., Chaisson, M., and Gingeras, T.R. (2013). STAR: ultrafast universal RNA-seq aligner. Bioinformatics *29*, 15–21.

Donovan, E.E., Pelanda, R., and Torres, R.M. (2010). S1P3 confers differential S1P-induced migration by autoreactive and non-autoreactive immature B cells and is required for normal B-cell development. Eur. J. Immunol. *40*, 688–698.

Filipenko, I., Schwalm, S., Reali, L., Pfeilschifter, J., Fabbro, D., Huwiler, A., and Zangemeister-Wittke, U. (2016). Upregulation of the S1P3 receptor in metastatic breast cancer cells increases migration and invasion by induction of PGE2 and EP2/EP4 activation. Biochim. Biophys. Acta *1861*, 1840–1851.

Forrest, M., Sun, S.Y., Hajdu, R., Bergstrom, J., Card, D., Doherty, G., Hale, J., Keohane, C., Meyers, C., Milligan, J., et al. (2004). Immune cell regulation and Cardiovascular effects of sphingosine 1-phosphate receptor agonists in rodents are mediated via distinct receptor subtypes. J. Pharmacol. Exp. Ther. *309*, 758–768.

Franken, N.A.P., Rodermond, H.M., Stap, J., Haveman, J., and van Bree, C. (2006). Clonogenic assay of cells in vitro. Nat. Protoc. *1*, 2315–2319.

Fulton, D., Gratton, J.P., McCabe, T.J., Fontana, J., Fujio, Y., Walsh, K., Franke, T.F., Papapetropoulos, A., and Sessa, W.C. (1999). Regulation of endothelium-derived nitric oxide production by the protein kinase Akt. Nature *399*, 597–601.

Galvani, S., Sanson, M., Blaho, V.A., Swendeman, S.L., Obinata, H., Conger, H., Dahlbäck, B., Kono, M., Proia, R.L., Smith, J.D., et al. (2015). HDL-bound sphingosine 1-phosphate acts as a biased agonist for the endothelial cell receptor S1P1 to limit vascular inflammation. Sci. Signal. *8*, ra79.

Ghandi, M., Huang, F.W., Jané-Valbuena, J., Kryukov, G.V., Lo, C.C., McDonald, E.R., Barretina, J., Gelfand, E.T., Bielski, C.M., Li, H., et al. (2019). Next-generation characterization of the cancer cell line Encyclopedia. Nature *569*, 503–508.

Ghosal, P., Sukocheva, O.A., Wang, T., Mayne, G.C., Watson, D.I., and Hussey, D.J. (2016). Effects of chemotherapy agents on Sphingosine-1-Phosphate receptors expression in MCF-7 mammary cancer cells. Biomed. Pharmacother. *81*, 218–224.

Gill, K.S., Fernandes, P., O'Donovan, T.R., McKenna, S.L., Doddakula, K.K., Power, D.G., Soden, D.M., and Forde, P.F. (2016). Glycolysis inhibition as a cancer treatment and its role in an anti-tumour immune response. Biochim. Biophys. Acta *1866*, 87–105.

Gupta, A., Anjomani-Virmouni, S., Koundouros, N., Dimitriadi, M., Choo-Wing, R., Valle, A., Zheng, Y., Chiu, Y.H., Agnihotri, S., Zadeh, G., et al. (2017). PARK2 depletion Connects energy and oxidative stress to PI3K/akt activation via PTEN S-nitrosylation. Mol. Cell *65*, 999–1013.e7.

Hanahan, D., and Weinberg, R.A. (2011). Hallmarks of cancer: the next generation. Cell *144*, 646–674.

Hauser, A.S., Attwood, M.M., Rask-Andersen, M., Schiöth, H.B., and Gloriam, D.E. (2017). Trends in GPCR drug discovery: new agents, targets and indications. Nat. Rev. Drug Discov. *16*, 829–842.

Hay, N. (2016). Reprogramming glucose metabolism in cancer: can it be exploited for cancer therapy? Nat. Rev. Cancer *16*, 635–649.

Heiden, M.G.V., Cantley, L.C., and Thompson, C.B. (2009). Understanding the Warburg effect: the metabolic requirements of cell proliferation. Science *324*, 1029–1033.

Hirayama, A., Kami, K., Sugimoto, M., Sugawara, M., Toki, N., Onozuka, H., Kinoshita, T., Saito, N., Ochiai, A., Tomita, M., et al. (2009). Quantitative metabolome profiling of colon and stomach cancer microenvironment by capillary electrophoresis time-of-flight mass spectrometry. Cancer Res. *69*, 4918–4925.

Inoue, A., Ishiguro, J., Kitamura, H., Arima, N., Okutani, M., Shuto, A., Higashiyama, S., Ohwada, T., Arai, H., Makide, K., et al. (2012). TGFα shedding assay: an accurate and versatile method for detecting GPCR activation. Nat. Methods *9*, 1021–1029.

Inoue, A., Raimondi, F., Kadji, F.M.N., Singh, G., Kishi, T., Uwamizu, A., Ono, Y., Shinjo, Y., Ishida, S., Arang, N., et al. (2019). Illuminating G-protein-coupling selectivity of GPCRs. Cell *177*, 1933–1947.e25.

Ito, K., and Suda, T. (2014). Metabolic requirements for the maintenance of self-renewing stem cells. Nat. Rev. Mol. Cell Biol. *15*, 243–256.

Jo, E., Bhhatarai, B., Repetto, E., Guerrero, M., Riley, S., Brown, S.J., Kohno, Y., Roberts, E., Schürer, S.C., and Rosen, H. (2012). Novel selective allosteric and bitopic ligands for the S1P3receptor. ACS Chem. Biol. *7*, 1975–1983.

Kenakin, T., and Christopoulos, A. (2013). Signalling bias in new drug discovery: detection, quantification and therapeutic impact. Nat. Rev. Drug Discov. *12*, 205–216.

Kii, I., Sumida, Y., Goto, T., Sonamoto, R., Okuno, Y., Yoshida, S., Kato-Sumida, T., Koike, Y., Abe, M., Nonaka, Y., et al. (2016). Selective inhibition of the kinase DYRK1A by targeting its folding process. Nat. Commun. *7*, 11391.

Kim, K.M., Han, C.Y., Kim, J.Y., Cho, S.S., Kim, Y.S., Koo, J.H., Lee, J.M., Lim, S.C., Kang, K.W., Kim, J.-S., et al. (2018). Gα12 overexpression induced by miR-16 dysregulation contributes to liver fibrosis by promoting autophagy in hepatic stellate cells. J. Hepatol. *68*, 493–504.

Koppenol, W.H., Bounds, P.L., and Dang, C.V. (2011). Otto Warburg's contributions to current concepts of cancer metabolism. Nat. Rev. Cancer *11*, 325–337.

Kunkel, G.T., MacEyka, M., Milstien, S., and Spiegel, S. (2013). Targeting the sphingosine-1-phosphate axis in cancer, inflammation and beyond. Nat. Rev. Drug Discov. *12*, 688–702.

Lappano, R., and Maggiolini, M. (2011). G protein-coupled receptors: novel targets for drug discovery in cancer. Nat. Rev. Drug Discov. *10*, 47–60.

Li, B., and Dewey, C.N. (2011). RSEM: accurate transcript quantification from RNA-Seq data with or without a reference genome. BMC Bioinformatics *12*, 323.

Lin, X., Zhang, F., Bradbury, C.M., Kaushal, A., Li, L., Spitz, D.R., Aft, R.L., and Gius, D. (2003). 2-Deoxy-D-glucose-induced cytotoxicity and radiosensitization in tumor cells is mediated via disruptions in thiol metabolism. Cancer Res. *63*, 3413–3417.

Love, M.I., Huber, W., and Anders, S. (2014). Moderated estimation of fold change and dispersion for RNA-seq data with DESeq2. Genome Biol. *15*, 1–21.

Madhavi Sastry, G., Adzhigirey, M., Day, T., Annabhimoju, R., and Sherman, W. (2013). Protein and ligand preparation: parameters, protocols, and influence on virtual screening enrichments. J. Comput. Aided Mol. Des. *27*, 221–234.

Manglik, A., Lin, H., Aryal, D.K., McCorvy, J.D., Dengler, D., Corder, G., Levit, A., Kling, R.C., Bernat, V., Hübner, H., et al. (2016). Structure-based discovery of opioid analgesics with reduced side effects. Nature *537*, 185–190.

Mizushima, N., Yoshimori, T., and Levine, B. (2010). Methods in mammalian autophagy research. Cell *140*, 313–326.

Nakano-Kobayashi, A., Awaya, T., Kii, I., Sumida, Y., Okuno, Y., Yoshida, S., Sumida, T., Inoue, H., Hosoya, T., and Hagiwara, M. (2017). Prenatal neurogenesis induction therapy normalizes brain structure and function in Down syndrome mice. Proc. Natl. Acad. Sci. U S A *114*, 10268–10273.

Nogueira, V., Park, Y., Chen, C.C., Xu, P.Z., Chen, M.L., Tonic, I., Unterman, T., and Hay, N. (2008). Akt determines replicative senescence and oxidative or oncogenic premature senescence and sensitizes cells to oxidative apoptosis. Cancer Cell *14*, 458–470.

Oslowski, C.M., Hara, T., O'Sullivan-Murphy, B., Kanekura, K., Lu, S., Hara, M., Ishigaki, S., Zhu, L.J., Hayashi, E., Hui, S.T., et al. (2012). Thioredoxin-interacting protein mediates ER stress-induced β cell death through initiation of the inflammasome. Cell Metab. *16*, 265–273.

O'Leary, N.A., Wright, M.W., Brister, J.R., Ciufo, S., Haddad, D., McVeigh, R., Rajput, B., Robbertse, B., Smith-White, B., Ako-Adjei, D., et al. (2016). Reference sequence (RefSeq) database at NCBI: current status, taxonomic expansion, and functional annotation. Nucleic Acids Res. *44*, D733–D745.

Pacini, P., Rinaldini, M., Algeri, R., Guarneri, A., Tucci, E., Barsanti, G., Neri, B., Bastiani, P., Marzano, S., and Fallai, C. (2000). FEC (5-fluorouracil, epidoxorubicin and cyclophosphamide) versus EM (epidoxorubicin and mitomycin-C) with or without lonidamine as first-line treatment for advanced breast cancer. A multicentric randomised study. Final results. Eur. J. Cancer *36*, 966–975.

Pavlova, N.N., and Thompson, C.B. (2016). The Emerging hallmarks of cancer metabolism. Cell Metab. *23*, 27–47.

Pearce, E.L., Poffenberger, M.C., Chang, C.-H., and Jones, R.G. (2013). Fueling immunity: insights into metabolism and lymphocyte function. Science *342*, 1242454.

Pieniazek, A., Czepas, J., Piasecka-Zelga, J., Gwoździński, K., and Koceva-Chyła, A. (2013). Oxidative stress induced in rat liver by anticancer drugs doxorubicin, paclitaxel and docetaxel. Adv. Med. Sci. *58*, 104–111.

Plas, D.R., and Thompson, C.B. (2005). Akt-dependent transformation: there is more to growth than just surviving. Oncogene *24*, 7435–7442.

Raez, L.E., Papadopoulos, K., Ricart, A.D., Chiorean, E.G., DiPaola, R.S., Stein, M.N., Rocha Lima, C.M., Schlesselman, J.J., Tolba, K., Langmuir, V.K., et al. (2013). A phase I dose-escalation trial of 2-deoxy-d-glucose alone or combined with docetaxel in patients with advanced solid tumors. Cancer Chemother. Pharmacol. *71*, 523–530.

Ramakrishnan, R., Huang, C., Cho, H. Il, Lloyd, M., Johnson, J., Ren, X., Altiok, S., Sullivan, D., Weber, J., Celis, E., et al. (2012). Autophagy induced by conventional chemotherapy mediates tumor cell sensitivity to immunotherapy. Cancer Res. *72*, 5483–5493.

Sako, Y., Ninomiya, K., Okuno, Y., Toyomoto, M., Nishida, A., Koike, Y., Ohe, K., Kii, I., Yoshida, S., Hashimoto, N., et al. (2017). Development of an orally available inhibitor of CLK1 for skipping a mutated dystrophin exon in Duchenne muscular dystrophy. Sci. Rep. *7*, 46126.

Sanna, M.G., Liao, J., Jo, E., Alfonso, C., Ahn, M.Y., Peterson, M.S., Webb, B., Lefebvre, S., Chun, J., Gray, N., et al. (2004). Sphingosine 1-phosphate (S1P) receptor subtypes S1P1 and S1P3, respectively, regulate lymphocyte recirculation and heart rate. J. Biol. Chem. *279*, 13839–13848.

Schrage, R., Schmitz, A.L., Gaffal, E., Annala, S., Kehraus, S., Wenzel, D., Büllesbach, K.M., Bald, T., Inoue, A., Shinjo, Y., et al. (2015). The experimental power of FR900359 to study Gq-regulated biological processes. Nat. Commun. *6*, 1–7.

Shibata, S., Ajiro, M., and Hagiwara, M. (2020). Mechanism-based personalized medicine for Cystic fibrosis by suppressing pseudo exon inclusion. Cell Chem. Biol. *27*, 1472–1482.e6.

Sultan, I., Qaddoumi, I., Yaser, S., Rodriguez-Galindo, C., and Ferrari, A. (2009). Comparing adult and pediatric rhabdomyosarcoma in the surveillance, epidemiology and end results program, 1973 to 2005: an analysis of 2,600 patients. J. Clin. Oncol. *27*, 3391–3397.

Takeshita, S., Kaji, K., and Kudo, A. (2000). Identification and characterization of the new osteoclast progenitor with macrophage phenotypes being able to differentiate into mature osteoclasts. J. Bone Miner. Res. *15*, 1477–1488.

Taniguchi, M., Kitatani, K., Kondo, T., Hashimoto-Nishimura, M., Asano, S., Hayashi, A., Mitsutake, S., Igarashi, Y., Umehara, H., Takeya, H., et al. (2012). Regulation of autophagy and its associated cell death by "sphingolipid rheostat": reciprocal role of ceramide and sphingosine 1-phosphate in the mammalian target of rapamycin pathway. J. Biol. Chem. *287*, 39898–39910.

Vander Heiden, M.G., and DeBerardinis, R.J. (2017). Understanding the intersections between metabolism and cancer biology. Cell *168*, 657–669.

Violin, J.D., Crombie, A.L., Soergel, D.G., and Lark, M.W. (2014). Biased ligands at G-protein-coupled receptors: promise and progress. Trends Pharmacol. Sci. *35*, 308–316.

Visentin, B., Vekich, J.A., Sibbald, B.J., Cavalli, A.L., Moreno, K.M., Matteo, R.G., Garland, W.A., Lu, Y., Yu, S., Hall, H.S., et al. (2006). Validation of an anti-sphingosine-1-phosphate antibody as a potential therapeutic in reducing growth, invasion, and angiogenesis in multiple tumor lineages. Cancer Cell *9*, 225–238.

Vrecl, M., Jorgensen, R., Pogačnik, A., and Heding, A. (2004). Development of a BRET2screening assay using β-arrestin 2 mutants. J. Biomol. Screen. *9*, 322–333.

Wang, D., and Dubois, R.N. (2010). Eicosanoids and cancer. Nat. Rev. Cancer *10*, 181–193.

Warburg, O. (1956). On the origin of cancer cells. Science *123*, 309–314.

Whalen, E.J., Foster, M.W., Matsumoto, A., Ozawa, K., Violin, J.D., Que, L.G., Nelson, C.D., Benhar, M., Keys, J.R., Rockman, H.A., et al. (2007). Regulation of β-adrenergic receptor signaling by S-nitrosylation of G-protein-coupled receptor kinase 2. Cell *129*, 511–522.

Windh, R.T., Lee, M.J., Hla, T., An, S., Barr, A.J., and Manning, D.R. (1999). Differential coupling of the sphingosine 1-phosphate receptors Edg-1, Edg-3, and H218/Edg-5 to the G(i), G(q), and G12 families of heterotrimeric G proteins. J. Biol. Chem. *274*, 27351–27358.

Wu, N., Zheng, B., Shaywitz, A., Dagon, Y., Tower, C., Bellinger, G., Shen, C., Wen, J., Asara, J., McGraw, T.E., et al. (2013). Short article AMPK-dependent degradation of TXNIP upon energy stress leads to enhanced glucose uptake via GLUT1. Mol. Cell *49*, 1167–1175.

Yamamoto, M., Onogi, H., Kii, I., Yoshida, S., Iida, K., Sakai, H., Abe, M., Tsubota, T., Ito, N., Hosoya, T., et al. (2014). CDK9 inhibitor FIT-039 prevents replication of multiple DNA viruses. J. Clin. Invest. *124*, 3479–3488.

Yang, J., Yan, R., Roy, A., Xu, D., Poisson, J., and Zhang, Y. (2015). The I-TASSER Suite: protein structure and function prediction. Nat. Methods *12*, 7–8.

Yu, F.X., Zhao, B., Panupinthu, N., Jewell, J.L., Lian, I., Wang, L.H., Zhao, J., Yuan, H., Tumaneng, K., Li, H., et al. (2012). Regulation of the Hippo-YAP pathway by G-protein-coupled receptor signaling. Cell *150*, 780–791.

Yu, O.M., Benitez, J.A., Plouffe, S.W., Ryback, D., Klein, A., Smith, J., Greenbaum, J., Delatte, B., Rao, A., Guan, K.L., et al. (2018). YAP and MRTF-A, transcriptional co-activators of RhoA-mediated gene expression, are critical for glioblastoma tumorigenicity. Oncogene *37*, 5492–5507.

Zheng, J. (2012). Energy metabolism of cancer: glycolysis versus oxidative phosphorylation (review). Oncol. Lett. *4*, 1151–1157.

Zhou, R., Tardivel, A., Thorens, B., Choi, I., and Tschopp, J. (2010). Thioredoxin-interacting protein links oxidative stress to inflammasome activation. Nat. Immunol. *11*, 136–140.

Zhou, Y., Zhou, B., Pache, L., Chang, M., Khodabakhshi, A.H., Tanaseichuk, O., Benner, C., and Chanda, S.K. (2019). Metascape provides a biologist-oriented resource for the analysis of systems-level datasets. Nat. Commun. *10*, 1523.

STAR★METHODS

KEY RESOURCES TABLE

REAGENT or RESOURCE	SOURCE	IDENTIFIER
Antibodies		
TXNIP (D5F3E) rabbit monoclonal antibody	Cell Signaling Technology	Cat# 14715; RRID: AB_2714178
LC3A/B (D3U4C) rabbit monoclonal antibody	Cell Signaling Technology	Cat# 13173; RRID: AB_2728823
beta-Tubulin (9F3) rabbit monoclonal antibody (HRP-conjugated)	Cell Signaling Technology	Cat# 5346; RRID: AB_1950376
Phospho-AMPK-alpha (Thr172) (40H9) rabbit monoclonal antibody	Cell Signaling Technology	Cat# 2535; RRID: AB_331250
AMPK-alpha (23A3) rabbit monoclonal antibody	Cell Signaling Technology	Cat# 2603; RRID: AB_490795
Phospho-Acetyl-CoA Carboxylase (Ser79) (D7D11) rabbit monoclonal antibody	Cell Signaling Technology	Cat# 11818; RRID: AB_2687505
Acetyl-CoA Carboxylase (C83B10) rabbit monoclonal antibody	Cell Signaling Technology	Cat# 3676; RRID: AB_2219397
Phospho-Akt (Ser473) (D9E) rabbit monoclonal antibody	Cell Signaling Technology	Cat# 4060; RRID: AB_2315049
Akt (40D4) mouse monoclonal antibody	Cell Signaling Technology	Cat# 2920; RRID: AB_1147620
Phospho-Stat1 (Tyr701) (58D6) rabbit monoclonal antibody	Cell Signaling Technology	Cat# 9167; RRID: AB_561284
Phospho-YAP (Ser127) (D9W2I) rabbit monoclonal antibody	Cell Signaling Technology	Cat# 13008; RRID: AB_2650553
YAP (D8H1X) rabbit monoclonal antibody	Cell Signaling Technology	Cat# 14074; RRID: AB_2650491
LATS1 (C66B5) rabbit monoclonal antibody	Cell Signaling Technology	Cat# 3477; RRID: AB_2133513
Vinculin (E1E9V) rabbit monoclonal antibody (HRP-conjugated)	Cell Signaling Technology	Cat# 18799; RRID: AB_2714181
Stat1 p84/p91 (C-136) mouse monoclonal antibody	Santa Cruz Biotechnology	Cat# sc-464; RRID: AB_675899
Phospho-Stat3 (Tyr705) (EP2147Y) rabbit monoclonal antibody	GeneTex	Cat# GTX61820; RRID: AB_10621431
gamma1-actin (2F3) mouse monoclonal antibody (HRP-conjugated)	FUJIFILM Wako Pure Chemical	Cat# 019-27833
Rat anti-rabbit IgG+IgM (SB87a) monoclonal antibody (HRP-conjugated)	abcam	Cat# ab99848; RRID: AB_10676047
Mouse TrueBlot ULTRA: Rat anti-mouse Ig monoclonal antibody (HRP-conjugated)	Rockland Immunochemicals	Cat# 18-8817-31; RRID: AB_2610850
LC3B (D11) rabbit monoclonal antibody	Cell Signaling Technology	Cat# 3868; RRID: AB_2137707
beta-Tubulin (1D4A4) mouse monoclonal antibody (CoraLite488-conjugated)	Proteintech Group	Cat# CL488-66240; RRID: AB_2883292
Rabbit (DA1E) IgG isotype control monoclonal antibody	Cell Signaling Technology	Cat# 3900; RRID: AB_1550038
Goat anti-Rabbit IgG (Alexa Fluor 647-conjugated)	Thermo Fisher Scientific	Cat# A-21245; RRID: AB_2535813
Chemicals, peptides, and recombinant proteins		
Chemical library of 696 in-house compounds	In house	N/A
ALESIA	In house	N/A
TrypLE express	Thermo Fisher Scientific	Cat# 12604-013
Hoechst 33342	DOJINDO LABORATORIES	Cat# H342

(*Continued on next page*)

Continued

REAGENT or RESOURCE	SOURCE	IDENTIFIER
Murine M-CSF	Peprotech PeproTech	Cat# 315-02
DAF-FM DA	GORYO Chemical	Cat# SK1004-01
Aminophenyl Fluorescein (APF)	GORYO Chemical	Cat# SK3002-02
CM-H2DCFDA dye	Thermo Fisher Scientific	Cat# C6827
DRAQ7	BioStatus	Cat# DR71000
Carboxy-PTIO	DOJINDO LABORATORIES	Cat# C348
L-NAME	Nacalai Tesque	Cat# 24540-61
Crystal violet	Nacalai Tesque	Cat# 09804-52
Myricetin	FUJIFILM Wako Pure Chemical	Cat# 137-16791
Coelenterazine h	FUJIFILM Wako Pure Chemical	Cat# 031-22993
2-Deoxy-D-glucose	Tokyo Chemical Industry	Cat# D0051-25G
Sphingosine 1-phosphate	Cayman Chemical	Cat# 62570
CYM 5541	Tocris Bioscience	Cat# 4897
CAY 10444	Cayman Chemical	Cat# 10005033
Critical commercial assays		
Viability/Cytotoxicity Assay Kit for Animal Live & Dead Cells	Biotium	Cat# 30002-T
TUNEL Assay Apoptosis Detection Kit	Biotium	Cat# 30074
Cell count reagent SF	Nacalai Tesque	Cat# 07553-44
RNeasy mini kit (250)	QIAGEN	Cat# 74106
RNase-free DNase set (50)	QIAGEN	Cat# 79254
iScript Reverse Transcription Supermix for RT-qPCR	Bio-Rad Laboratories	Cat# 1708841
SYBR premix Ex Taq (Tli RNaseH Plus)	Takara Bio	Cat# RR420A
NucView488 and RedDot2 Apoptosis and Necrosis Kit	Biotium	Cat# 30072
CelLytic M	Sigma-Aldrich	Cat# C2978
Blocking One solution	Nacalai Tesque	Cat# 03953-95
Can Get Signal immunoreaction Enhancer Solution	Toyobo	Cat# NKB-101
ImmunoStar LD	FUJIFILM Wako Pure Chemical	Cat# 290-69904
NADP/NADPH Extraction Buffer	BioVision	Cat# K347-100-1
NADP/NADPH-Glo Assay	Promega	Cat# G9081
Pierce 660nm Protein Assay Reagent	Thermo Fisher Scientific	Cat# 22660
Glucose Colorimetric Assay Kit	Cayman Chemical	Cat# 10009582
Deposited data		
RNA-seq RAW and analyzed data	This paper	GEO: GSE143670
Refseq GRCh37.p5	O'Leary et al., 2016	PMID: 26553804
Cancer Cell Line Encyclopedia	Ghandi et al., 2019	PMID: 31068700
Experimental models: cell lines		
Human: MIA PaCa-2 cells	JCRB	JCRB0070
Human: HeLa cells	JCRB	JCRB9004
Human: MCF-7 cells	JCRB	JCRB0134
Human: Normal Human Dermal Fibroblasts (NHDF), juvenile foreskin	PromoCell	C-12300
Human: C33A cells	ATCC	HTB-31
Human: GLuc-stable C33A cells	Ajiro et al., 2018	PMID: 29712686
Human: A-204 cells	ATCC	HTB-82

(*Continued on next page*)

Continued

REAGENT or RESOURCE	SOURCE	IDENTIFIER
Human: GLuc-stable A-204 cells	This paper	N/A
Mouse: CMG14-12 cells	Takeshita et al., 2000	PMID: 10934646
Human: HEK293 cells (parental HEK293) cells	Inoue et al., 2012	PMID: 22983457
Human: ΔGq HEK293 cells	Schrage et al., 2015	CL1; PMID: 26658454
Human: ΔG12 HEK293 cells	Devost et al., 2017	CL3; PMID: 28213525
Human: ΔGq/ΔG12 HEK293 cells	Devost et al., 2017	CL4-1; PMID: 28213525
Experimental models: organisms/strains		
Mouse: C57BL/6JmsSlc	Japan SLC	N/A
Mouse: BALB/cCrSlc	Japan SLC	N/A
Mouse: BALB/c Slc-nu/nu	Japan SLC	N/A
Mouse: C.B-17/IcrHsd-Prkdcscid	Japan SLC	N/A
Oligonucleotides		
TXNIP, forward, 5′-CAGCCAACAGGTGAGAATGA-3′	Oslowski et al., 2012	PMID: 22883234
TXNIP, reverse, 5′-TTGAAGGATGTTCCCAGAGG-3′	Oslowski et al., 2012	PMID: 22883234
ACTB, forward, 5′-TTGGCAATGAGCGGTTCC-3′	Cao et al., 2012	PMID: 22995308
ACTB, reverse, 5′-GTTGAAGGTAGTTTCGTGGATG-3′	Cao et al., 2012	PMID: 22995308
Recombinant DNA		
Plasmid: pJTI Fast DEST	Thermo Fisher Scientific	Cat# A10894
Plasmid: pJTI PhiC31 Int	Thermo Fisher Scientific	Cat# A10894
cDNA GLuc	NanoLight Technology	Cat# 202 pCMV-Gluc
Human GPCR-encoding plasmids library	Inoue et al., 2012	PMID: 22983457
AP-TGF-α (codon-optimized)	Inoue et al., 2012	PMID: 22983457
Chimeric Gα subunits	Inoue et al., 2012	PMID: 22983457
NanoBiT-G-proteins	Inoue et al., 2019	PMID: 31160049
Software and algorithms		
Harmony 4.9	PerkinElmer	https://www.perkinelmer.com
STAR aligner ver. 2.4.1d	Dobin et al., 2013	PMID: 23104886
RSEM ver. 1.3.0	Li & Dewey, 2011	PMID: 21816040
DESeq2 package ver. 1.8.2	Love et al., 2014	PMID: 25516281
FlowLogic 6.0	Inivai Technologies	https://www.inivai.com
Image Lab software	Bio-Rad Laboratories	https://www.bio-rad.com
GraphPad Prism 6, 7, or 8	GraphPad Software	https://www.graphpad.com
Cell3iMager software version 2.4	SCREEN Holdings	https://www.screen-cell3imager.com
I-TASSER server	Yang et al., 2015	PMID: 25549265
Schrödinger suite 2017-01	Madhavi Sastry et al., 2013	PMID: 23579614
LigPrep tool	Schrödinger	https://www.schrodinger.com
Glide	Schrödinger	https://www.schrodinger.com
R software ver. 4.0	R Development Core Team	https://www.r-project.org
Metascape	Zhou et al., 2019	PMID: 30944313

RESOURCE AVAILABILITY

Lead contact

Further information and requests for resources and reagents should be directed to and will be fulfilled by the Lead Contact, Masatoshi Hagiwara (hagiwara.masatoshi.8c@kyoto-u.ac.jp <mailto:hagiwara.masatoshi.8c@kyoto-u.ac.jp>).

Materials availability

Correspondence and requests for materials should be addressed to the Lead Contact. ALESIA is available from M.H. for research purposes under a material transfer agreement with Kyoto University.

Data and code availability

All data are available in the main text or as Supplemental information. RNA-seq data generated in this study have been deposited in the Gene Expression Omnibus (accession no. GSE143670).

EXPERIMENTAL MODEL AND SUBJECT DETAILS

Animals

Mice were co-housed at 3–5 mice per cage and maintained under pathogen-free conditions on a 12-h light/dark cycle facility with access to food and water ad libitum. For all *in vivo* experiments, animals were allowed to acclimate for a minimum of 7 days prior to manipulation. All animal protocols were reviewed and approved by the Animal Research Committee, Graduate School of Medicine, Kyoto University, and the studies were conducted in accordance with the Regulation on Animal Experimentation of Kyoto University.

Cell lines

MIA PaCa-2 (male), HeLa (female), and MCF-7 (female) cells were obtained from JCRB (Osaka, Japan). Normal human dermal fibroblasts (NHDFs; male) were obtained from PromoCell (Heidelberg, Germany). HEK293A (female) cells were purchased from Thermo Fisher (Waltham, MA, USA). C33A (female) and A-204 (female) cells were obtained from the American Type Culture Collection (ATCC, Manassas, VA, USA). MIA PaCa-2, HeLa, NHDFs, and A-204 were cultured in MEM (Nacalai Tesque, Kyoto, Japan) containing 5 % (v/v) heat-inactivated FBS (Thermo Fisher), 100 U/ml penicillin, and 100 μg/ml streptomycin (Nacalai Tesque). MCF-7, C33A, HEK293A, and G protein-deficient HEK293A cells (ΔGq, ΔG12, and ΔGq/ΔG12) (Devost et al., 2017; Schrage et al., 2015) were cultured in DMEM (1 g/l glucose; Nacalai Tesque) containing 10 % (v/v) FBS, 100 U/ml penicillin, and 100 μg/ml streptomycin (complete DMEM). All cells were incubated under standard conditions (37 °C, 5 % CO_2).

Primary cultures

Murine bone marrow cells were isolated from 8-week-old male C57BL/6J mice (Japan SLC, Shizuoka, Japan) and cultured for 8 days in DMEM (4.5 g/l glucose; Nacalai Tesque) supplemented with 10 % (v/v) FBS, 100 U/ml penicillin, 100 μg/ml streptomycin, and 10 % (v/v) culture supernatant of macrophage colony-stimulating factor–producing and secreting CMG14-12 (male) cells (Takeshita et al., 2000) to generate murine bone marrow-derived macrophages. All cells were incubated under standard conditions (37 °C, 5 % CO_2).

Preparation of Gaussia luciferase (GLuc)-stable C33A cells for xenograft tumor formation

A modified pJTI Fast DEST expression vector (Thermo Fisher; containing GLuc cDNA under the control of the CAGGS promoter, pseudo attB site, and hygromycin B resistance gene) was used with a ϕC31 integrase expression vector (pJTI PhiC31 Int; Thermo Fisher) to co-transfect C33A cells using Lipofectamine 2000 reagent (Thermo Fisher). The transfected cells were cultured in the presence of 600 μg/ml hygromycin B for 2 weeks, and the resulting single colonies were isolated.

Xenograft model

Five-week-old female nude mice (BALB/c Slc-nu/nu, 15–20 g) were purchased from the Japan SLC (Shizuoka, Japan). Cultured GLuc-stable C33A cells (Ajiro et al., 2018) were suspended in HBSS at a density of 2×10^7 cells/ml. Next, 100 μl (1×10^6) of GLuc-stable C33A cells in a 1:1 mixture with Matrigel (BD Bioscience) were transplanted subcutaneously on both flanks of isoflurane-anesthetized mice. Tumor volumes were calculated every 3 or 4 d using calliper measurements and the following formula: $V = (LW^2)/2$; where V is the volume (mm^3); L is the largest diameter (mm); and W is the smallest diameter (mm). ALESIA was formulated in the vehicle [saline with 20 % (w/w) PEG400, 20 % (w/w) olive oil, 3 % (w/w) Tween 80, and 100 mg/ml 2DG] and the mice received oral doses of the 2DG alone or 2DG with ALESIA (200 mg/kg), daily, by gavage.

Preparation of GLuc-stable A-204 cells for intraperitoneal dissemination xenograft model

A modified pJTI Fast DEST expression vector (Thermo Fisher; containing the GLuc cDNA under the control of the CAGGS promoter, pseudo attB site, and hygromycin B resistance gene) was used with a ϕC31 integrase expression vector (pJTI PhiC31 Int; Thermo Fisher) to co-transfect A-204 cells by using FuGENE HD reagent. The transfected cells were cultured in the presence of 300 μg/ml hygromycin B (Nacalai Tesque) for 2 weeks, and the resulting single colonies were isolated.

Xenograft model with intraperitoneal dissemination

Five-week-old female SCID mice (C.B-17/IcrHsd-*Prkdc*^{scid}) were purchased from the Japan SLC (Shizuoka, Japan). Cultured GLuc-stable A-204 cells were suspended in HBSS at a density of 5×10^6 cells/ml. Next, 1 ml (5×10^6) of GLuc-stable A-204 cells were transplanted intraperitoneally in mice. ALESIA was suspended in a vehicle [saline containing 0.05 % (w/w) Tween 80] using 3-mm stainless beads and μT-12 bead crusher (TAITEC, Saitama, Japan) at 1800 rpm for 5 min. The mice received intraperitoneal administration of the vehicle alone or ALESIA (50 mg/kg, 10 ml/kg) 5 times a week.

METHOD DETAILS

Plasmid construction

For the NanoBiT–β-arrestin recruitment assay (Dixon et al., 2016), a receptor construct was designed to fuse the small fragment (SmBiT) of the NanoBiT complementation luciferase sequence to the C-terminus of human S1PR3 with a 15-amino acid flexible linker (GGSGGGGSGGSSSGG), whose sequence was recommended by the manufacturer (Promega, Madison, WI, USA). The construct (HA-S1PR3-SmBiT) was assembled and inserted into a pCAGGS mammalian expression plasmid (a kind gift from Dr. Jun-ichi Miyazaki, Osaka University). β-arrestin construct was generated by fusing the large fragment (LgBiT), whose nucleotide sequence was synthesized after mammalian codon optimization (Genscript, Piscataway, NJ, USA), with the N-terminus of the human β-arrestin1 or β-arrestin2 using the 15-amino acid linker. To enhance the β-arrestin recruitment signal, amino acid substitutions to create protein variants unable to bind AP-2 were introduced in β-arrestin1 (R393E and R395E) and β-arrestin2 (R393E and R395E) (Vrecl et al., 2004).

In *vitro* phenotypic screening

The screening was performed against our chemical library of 696 in-house compounds (Kii et al., 2016; Nakano-Kobayashi et al., 2017; Sako et al., 2017; Shibata et al., 2020; Yamamoto et al., 2014). MIA PaCa-2 cells were seeded into CellCarrier-96 ultra (PerkinElmer, Waltham, MA, USA). For the primary screen, 10,000 cells were seeded per well in low-glucose medium (0.05 g/l glucose) or normal-glucose medium (1.0 g/l glucose) and then allowed to attach overnight. The next day, test compounds from an original library were placed in assay plates, which resulted in a final drug screening concentration of 10 μM. DMSO vehicle controls and cell-free blank controls were included in each assay plate. The cells were incubated for 1 day, after which they were fixed with 1.5 % (w/v) PFA. Fixed cells were imaged using the Opera Phenix high-content screening system (Opera; PerkinElmer). A set of 25 fields (646 μm × 646 μm per field) was visualized in each well by digital phase contrast with a 20× water-immersion objective. The number of adherent cells was calculated by using Harmony 4.6 software (PerkinElmer) and normalized to 100, for DMSO-treated wells, and 0, for cell-free blank wells, on a per plate basis.

Cell proliferation and cytotoxicity assay

Cell viability was determined using the cell count reagent SF (Nacalai Tesque) according to the manufacturer's instructions.

Cell viability assays

Cells were seeded in the PureCoat Amine 96-well plate (Corning Inc., Corning, NY, USA). Cell viability was determined using the viability/cytotoxicity assay kit for animal live and dead cells (Biotium, Fremont, CA, USA), according to the manufacturer's instructions. The nuclei were visualized by Hoechst 33342 staining (Dojindo, Kumamoto, Japan; 5 μg/ml). Stained cells were imaged using the Opera with a 20× water-immersion objective in confocal mode and collected with a set of 25 fields from each well. Hoechst-positive, calcein-positive, and ethidium homodimer III (EthDIII)–negative cells were counted as viable cells by using Harmony 4.6 software.

Apoptotic cell analysis

HeLa cells were stained using the CF640R TUNEL assay apoptosis detection kit (Biotium) and Hoechst 33342, according to the manufacturers' instructions. Stained cells were imaged using the Opera, with a set of 25 fields collected from each well. Hoechst-positive and TUNEL-positive cells were counted as TUNEL-positive cells by using Harmony 4.6 software.

RNA-sequencing (RNA-seq) experiment and data analysis

Cells were treated with the test compound for 6 h. RNA was purified using the RNeasy mini kit (QIAGEN, Hilden, Germany) with RNase-free DNase set (QIAGEN). RNA quality for sequencing was determined using the 2100 Bioanalyzer (Agilent, Santa Clara, CA, USA); in all samples, the RNA integrity number (RIN) was > 9.

For transcriptome analysis of HeLa cells, RNA-Seq libraries were prepared using the TruSeq Stranded mRNA (Illumina, San Diego, CA) from the purified RNA. The libraries were then used for paired-end sequencing with the Illumina NovaSeq 6000 platform.

For transcriptome analysis of MCF-7 cells, 10 μg of total RNA mixed with 2 μl of a diluted ERCC RNA spike-in mix (1:10 diluted; Thermo Fisher) was poly-A purified using Dynabeads mRNA DIRECT micro kit (Thermo Fisher). The poly-A–purified RNA was used for RNA-seq library preparation using the Ion Total RNA-seq kit for the AB Library Builder System (Thermo Fisher). The prepared libraries were purified using Agencourt AMPure XP (Beckman Coulter, Brea, CA, USA). Single-end sequencing was performed using the Ion Proton System. Sequenced reads were discarded if they were shorter than 50 nt, their average quality scores were below 17, or they were derived from RNA elements (rRNA, tRNA, snRNA, or snoRNA) or repetitive regions (Bao et al., 2015).

The remaining mRNA-seq reads were mapped to the human genome sequence (hg19) using the STAR aligner ver. 2.4.1d using ENCODE standard options (Dobin et al., 2013). For the gene annotation, Refseq GRCh37.p5 was used (O'Leary et al., 2016). Transcripts per million (TPM) values and raw read counts were calculated using RSEM ver. 1.3.0 (Li and Dewey, 2011). Differentially expressed genes were identified using the DESeq2 package ver. 1.8.2 in Bioconductor (Love et al., 2014). When TPM $\geq$ 1 and raw read counts $\geq$ 31, the genes were treated as expressed. Differentially expressed genes were then defined using the threshold for

fold-changes $\geq$ 1.3 and the adjusted p-value < 0.05. In figures and tables, only protein-coding genes are shown. Genes from the cytochrome P450 gene superfamily were excluded from the differentially expressed gene set.

The Venn diagrams were generated by using the website "Bioinformatics & Evolutionary Genomics" (http://bioinformatics.psb.ugent.be/webtools/Venn/).

QuantitativeRT-PCR (RT-qPCR)

RNA was isolated using the RNeasy mini kit (QIAGEN) with RNase-free DNase set (QIAGEN). Then, cDNA was synthesized from 1 μg of total RNA using the iScript reverse transcription supermix for RT-qPCR (Bio-Rad). The obtained cDNA was mixed with the specified primers and SYBR premix Ex Taq (Tli RNaseH Plus; Takara Bio). RT-qPCR was then performed using the StepOne Plus Real-Time PCR system (Thermo Fisher). Relative quantification was performed with data normalized to β-actin (ACTB) mRNA expression. The following primers were used in the current study: *TXNIP*, forward, 5′-CAGCCAACAGGTGAGAATGA-3′, and reverse, 5′-TTGAAGGATGTTCCCAGAGG-3′ (Oslowski et al., 2012); and *ACTB*, forward, 5′-TTGGCAATGAGCGGTTCC-3′, and reverse, 5′-GTTGAAGGTAGTTTCGTGGATG-3′ (Cao et al., 2012).

Immunoblotting

Cells were lysed using CelLytic M (Sigma, St. Louis, MO, USA) containing protease inhibitor cocktail (Nacalai Tesque) and phosphatase inhibitor cocktail (Nacalai Tesque). Cell lysates were mixed with sample buffer solution (Nacalai Tesque), denatured at 95 °C for 10 min, separated by SDS-PAGE, and transferred onto Immobilon-P membranes (Merck, Burlington, MA, USA). Membranes were blocked overnight in 50 % (v/v) Blocking One solution (Nacalai Tesque) in TBS-T buffer (Takara Bio). Antibody reactions were performed using the Can Get Signal immunoreaction enhancer solution (Toyobo, Osaka, Japan). Peroxidase activity was visualized using ImmunoStar LD (Wako, Osaka, Japan) and ChemiDoc MP imaging system (Bio-Rad, Hercules, CA, USA). The following primary antibodies were used [unless specified otherwise, all were from Cell Signaling Technology (Danvers, MA, USA) and used at a dilution of 1:5000]: rabbit anti-TXNIP (clone D5F3E), rabbit anti-LC3A/B (clone D3U4C, 1:2000), HRP-conjugated rabbit anti-β-tubulin (clone 9F3), rabbit anti-phospho-AMPKα (clone 40H9), rabbit anti-AMPKα (clone 23A3), rabbit anti-phospho-ACC (Ser79; clone D7D11), rabbit anti-ACC (clone C83B10), rabbit anti-phospho-AKT (Ser473; clone D9E), mouse anti-AKT (clone 40D4), rabbit anti-phospho-STAT1 (Tyr701; clone 58D6), mouse anti-STAT1 (clone C-136, 1:1000; Santa Cruz Biotechnology), rabbit anti-phospho-STAT3 (Tyr705; clone EP2147Y; GeneTex, Irvine, CA, USA), rabbit anti-phospho-YAP (Ser127; clone D9W2I), rabbit anti-YAP (clone D8H1X, 1:2500), rabbit anti-LATS1 (clone C66B5), HRP-conjugated mouse anti-γ1-actin (clone 2F3, 1:20000; Wako), and HRP-conjugated rabbit anti-vinculin (clone E1E9V).

Determination of intracellular nitric oxide

Intracellular NO production was determined using DAF-FM diacetate (GORYO Chemical, Hokkaido, Japan) fluorescent dye. After treatment with the test compound, the cells were loaded with 1 μM DAF-FM diacetate in HBSS (Nacalai Tesque) for 30 min at 37 °C. The cells were detached using TrypLE express (Thermo Fisher), and analysed using the Accuri C6 flow cytometer (BD Biosciences) and FlowLogic 6.0 software (Inivai Technologies, Victoria, Australia).

Determination of intracellular reactive oxygen species

Intracellular ROS production was determined using APF fluorescent dye (GORYO Chemical) or CM-H_2DCFDA dye (Thermo Fisher), with the analysis conducted by using the Accuri C6.

Determination of caspase-3 activity

Caspase-3 activity was determined using the NucView488 and RedDot2 apoptosis and necrosis kit (Biotium), according to the manufacturer's instructions. Dead cells were stained with RedDot2 or DRAQ7 (BioStatus, Shepshed, UK). HeLa cells were incubated with the vehicle, 0.2 mM cPTIO (Dojindo), or 4 mM L-NAME (Nacalai Tesque) for 1 h before L-c414 was added. The data were analyzed by using the Accuri C6.

In *vitro* kinase assay

For the assay, 0.5 ng/μl full-length recombinant human AMPKα1β1γ1 (SignalChem, Richmond, BC, Canada) was incubated for 60 min with 0.2 μg/μl of SAMS peptide (Abcam, Cambridge, UK) and 150 μM ATP in the kinase assay buffer [2.5 mM MOPS (pH 7.2), 1.25 mM β-glycerol-phosphate, 2.5 mM $MgCl_2$, 0.5 mM EGTA, 0.2 mM EDTA, 0.25 mM DTT, 0.01 % (w/v) Brij-35, 0.25 % (w/v) bovine serum albumin (BSA), and 0.125 % (w/v) Tween 80] at 25 °C. ATP hydrolysis resulting from the kinase reactions was detected using the ADP-Glo kinase assay kit (Promega).

TGFα shedding assay

TGFα shedding assay for the determination of ectodomain shedding of alkaline phosphatase (AP)-tagged TGFα (AP-TGFα) induced by G_q and G_{12} signals was performed as described previously (Inoue et al., 2012), with minor modifications. Briefly, parent HEK293A cells and G protein-deficient (G_q-deficient, G_{12}-deficient, and G_q/G_{12}-deficient) HEK293A cells (Devost et al., 2017; Schrage et al., 2015) were seeded in a 10-cm culture dish at 2 × 10^6 cells (all cell lines) or 2.5 × 10^6 cells (G_q/G_{12}-deficient cells) in 10 ml of complete DMEM, and cultured for 1 day in a CO_2 incubator. A mixture of AP-TGFα reporter

plasmid (2.5 μg) and plasmid encoding human untagged $S1P_3$ (1 μg) were used for transfection by diluting in 500 μl of Opti-MEM I reduced serum medium (Thermo Fisher), and combining with 25 μl of 1 mg/ml PEI reagent (polyethylenimine "Max", mol wt 40,000; Polysciences, Warrington, PA, USA) diluted in 500 μl of the Opti-MEM medium. The transfected cells were detached with PBS containing 0.05 % (w/v) trypsin and 0.52 mM EDTA, and collected in a 50-ml tube, and harvested by centrifugation at 190 × *g* for 5 min. The cell pellet was resuspended in Dulbecco's PBS (D-PBS), followed by incubation for 15 min at 26 °C. After a second centrifugation at 190 × *g* for 5 min, the pelleted cells were resuspended in 30 ml of HBSS containing 5 mM HEPES (pH 7.4). The cell suspensions were plated at 90 μl per well in a 96-well plate and incubated at 37 °C with 5 % CO_2 for 30 min. When the experiments were performed using S1PR3 agonists, the cells were seeded in a 10-cm dish in 10 ml of medium, and 5-fold volume of reagents was used in the subsequent procedures until cell seeding into the 96-well plate. After the equilibration period, 10 μl per well of 10× concentrated solutions of test compounds diluted in HBSS containing 0.01 % (w/v) BSA (fatty acid-free grade; SERVA Electrophoresis, Heidelberg, Germany) were added, and incubated for 1 h at 37 °C with 5 % CO_2. Plates were centrifuged at 190 × *g* for 2 min; the cells were retained and 80 μl of the supernatant was transferred to another 96-well plate. A solution containing *p*-nitrophenyl phosphate (*p*-NPP) [10 mM p-NPP, 40 mM Tris-HCl (pH 9.5), 40 mM NaCl, and 10 mM $MgCl_2$] was added (80 μl per well) to the supernatant and cell plates. Absorbance at 405 nm of both plates was read before and after 1-h incubation at 26 °C, using a microplate reader (VersaMax, Molecular Devices, San Jose, CA, USA). G protein signal activation was expressed as a relative amount of AP-TGFα reporter released into the conditioned media from baseline release signal (Inoue et al., 2012). AP-TGFα release was calculated by subtracting the spontaneous AP-TGFα accumulation under the vehicle-treated conditions from that under the compound-stimulated conditions. At each S1PR3 agonist concentration, the receptor-specific signal was determined by subtracting AP-TGFα release in mock-transfected cells from that in S1PR3-transfected cells.

The ligand-induced signals determined in the TGFα shedding assay with various concentrations of S1PR3 agonists were fitted to a four-parameter sigmoidal concentration-response curve, using the GraphPad Prism 7 software (GraphPad Software, La Jolla, CA, USA). The fitted concentration-response curve was used to obtain the pEC_{50} (equal to -log10 EC_{50}) and E_{max} values.

NanoBiT–β-arrestin recruitment assay

HEK293A cells were seeded in a 10-cm dish (2 × 10^6 cells in 10 ml of complete DMEM) and cultured for 1 day. The cells were transfected with a mixture of S1PR3–SmBiT plasmid (1 μg) and LgBiT–β-arr plasmid (LgBiT–β-arr1 or LgBiT–β-arr2; 500 ng) by diluting in 500 μl of Opti-MEM (Thermo Fisher), and combining with 25 μl of 1 mg/ml PEI MAX (Polysciences) reagent diluted in 500 μl of the Opti-MEM. As a negative control, the pCAGGS plasmid was used instead of the S1PR3-SmBiT plasmid. After the addition of the transfection solution (after 24 h), the cells were harvested in 5 ml of D-PBS containing 0.53 mM EDTA, which was followed by rinsing with 5 ml of HBSS containing 5 mM HEPES (pH 7.4). The cells were centrifuged at 190 × *g* for 5 min and suspended in 10 ml of HBSS containing 0.01 % (w/v) BSA (BSA-HBSS). The cell suspension was seeded in a 96-well white plate (80 μl per well) and 20 μl of 50 μM coelenterazine (Carbosynth, Compton, UK) in BSA-HBSS was added per well. After incubation at 26 °C for 2 h, the background luminescent signals were measured using a luminescent microplate reader (SpectraMax L equipped with two detectors, Molecular Devices). Then, 20 μl of 6 × concentrated test compounds were added; 5 min after the addition of ligands, luminescent signals were measured for 5 min at 20-s intervals. For each well, the luminescent signal was normalized to the initial count, and fold-change values over 5–10 min after ligand stimulation were averaged. For fitting analysis, fold-change luminescent signals were fitted to a four-parameter sigmoidal curve using the Prism 7, and EC_{50} and E_{max} values were obtained from the curves according to the manufacturer's instructions.

NADPH measurements

Cells were lysed in NADP/NADPH extraction buffer (BioVision, Milpitas, CA, USA) for 10 min on ice. Protein concentrations were determined using the 660-nm protein assay reagent (Thermo Fisher). To detect the reduced form (NADPH) only, the lysates were incubated at 60 °C for 30 min. Thereafter, NADP/NADPH-Glo assay (Promega) was used for NADPH determination. Sample absorbance or luminescence was recorded using the ARVO X5 multimode plate reader (PerkinElmer).

Glucose assay

Glucose concentrations in the culture supernatants were determined using the glucose colorimetric assay kit (Cayman, Ann Arbor, MI, USA). Data were normalized to glucose concentration in the culture medium before culturing.

Clonogenic cell survival assay

HeLa or A-204 cells were plated 200 cells/well in a 6-well plate and then allowed to attach overnight. The next day, compounds were placed in the plates at various concentrations. In the case of multi-compound treatment, 1 mM L-NAME or 6 μM myricetin (Wako) was added into the plate, and then ALESIA was. The HeLa or A-204 cells were incubated for 14 days or 28 days respectively, after which they were fixed and stained with 0.25 % crystal violet (Nacalai Tesque) and 25 % methanol in PBS at RT (20–26 °C) for 30 min. The wells were washed with water once and dried at RT. The wells were imaged using the Cell^{3}iMager CC-5000 (SCREEN Holdings, Kyoto, Japan). All images were scanned with a resolution of 2400 dpi. The colonies over 400 μm in diameter were defined as survival and the number of them was calculated by using Cell3iMager software version 2.4 (SCREEN Holdings).

Immunofluorescent analysis

HeLa cells in a PureCoat Amine 96-well plate were fixed with 4% PFA for 20 min at RT and washed with PBS once, and then they were fixed with ice-cold methanol for 20 min at -30 °C and washed with PBS twice. The cells were then permeabilized using 0.1 % (w/w) Triton X-100 (Sigma) for 5 min and washed with PBS twice. A solution containing 1 % (w/v) BSA and 2.5 % (v/v) normal goat serum was next added onto the wells, as a blocking solution, and kept for 30 min at RT. The blocking solution was removed from the wells and the rabbit anti-LC3B antibodies (clone D11; Cell Signaling Technology) at 500-fold dilutions in Can Get Signal immunostain Solution A were added in the wells. The wells with primary antibodies were incubated at 4 °C for 16–24 h and then washed three times with PBS containing 0.1 % Triton X-100. Subsequently, the wells were incubated at RT for 1 hour with a PBS containing 1 % BSA, 0.1 % Triton X-100, 5 μg/ml Hoechst 33342, 1,000-fold diluted CoraLite488-conjugated mouse anti-β tubulin antibody (Proteintech, Rosemont, IL, USA), and 200-fold diluted Alexa Fluor 647-conjugated goat anti-rabbit IgG secondary antibodies (Thermo Fisher). Finally, wells were washed 3 times with PBS containing 0.1 % Triton X-100. The stained cells were imaged using the Opera in confocal mode with 63× water-immersion objective and a set of 81 fields (205 μm × 205 μm per field) was captured in each well. LC3-positive dots per Hoechst-positive cells were counted as LC3 puncta per cell by using Harmony 4.9 software.

Histology and TUNEL staining

Formalin-fixed paraffin-embedded tumor tissues were sectioned at 3-μm, thickness and stained with H&E. The CF640R TUNEL assay apoptosis detection kit (Biotium) and Hoechst 33342 were used for TUNEL staining according to the manufacturer's instructions.

GLuc serum assay

Murine blood samples were collected by making a small incision using a lancet in the submandibular vein of awake mice. After collection, the blood samples were allowed to clot by leaving undisturbed at RT for 30 min, and then incubating at 4 °C overnight. The samples were then centrifuged to remove the clot. The resulting supernatant was the serum sample. For the GLuc assay, typically, 5 μl of the serum was added to 45 μl of D-PBS containing 0.02 % (w/w) Tween 20 and 20 mM EDTA. GLuc activity was measured using Centro LB 960 microplate luminometer (Berthold Technologies, Bad Wildbad, Germany) set to inject 50 μl of 20 μg/ml coelenterazine h (Wako) in the above buffer and to acquire photon counts for 12 s.

GLuc assay

Murine blood samples were collected in capillary blood collection tubes with EDTA by making a small incision using a scalpel in the tail vein of awake mice. After collection, the blood samples were centrifuged to remove the clot. The resulting supernatant was the plasma sample. For the GLuc assay, typically, 5 μl of the plasma was added to 45 μl of D-PBS containing 0.02 % (w/w) Tween 20 and 20 mM EDTA. GLuc activity was measured using the ARVO X5 multimode plate reader (PerkinElmer) after injecting 50 μl of 20 μg/ml coelenterazine h (Wako) in the above buffer.

Cancer panel

Cell preparation: All cell lines have been licensed from the American Type Culture Collection (ATCC, Manassas, VA, USA). Master and working cell banks (MCB and WCB, respectively) were prepared by sub-culturing in the ATCC-recommended media and freezing, according to the protocols recommended by the ATCC. Cell line stocks for the assays were prepared from the WCB. The MCB, WCB, and assay stocks were prepared within 3, 6, and 9 passages, respectively, from the ATCC vials.

Compound preparation: A compound was weighed using a calibrated balance and dissolved in 100 % DMSO. The samples in DMSO were then stored at RT. On the day of the experiment, the compound stock was diluted in 3.16-fold steps in 100 % DMSO to obtain a 9-point dilution series. The series was further diluted 31.6-times in 20 mM sterile HEPES buffer, pH 7.4. Then, 5 μl of the dilution was added to the cells, to generate a test concentration range from 3.16×10^{-5} M to 3.16×10^{-9} M, in duplicate. The final DMSO concentration during incubation was 0.4 % (v/v) in all wells.

Cell proliferation assay: An assay stock was thawed, diluted in the ATCC-recommended medium, and dispensed into a 384-well plate, at a concentration of 400–1600 cells per well in 45 μl of the medium. Cell density optimal for each cell line was used. The wells in plate margins were filled with PBS. The plated cells were incubated in a humidified atmosphere of 5 % CO_2 at 37 °C. After 24 h, 5 μl of the compound dilution was added, and the plates were incubated for additional 72 h. After 72 h, 25 μl of ATPlite 1step (PerkinElmer) solution was added to each well, and the plates were shaken for 2 min. After 10 min of incubation in the dark, the luminescence was recorded using an Envision multimode reader (PerkinElmer).

Controls: Signal at time 0: In parallel, 45 μl of cells were dispensed and incubated in a humidified atmosphere of 5 % CO_2 at 37 °C. After 24 h, 5 μl of DMSO-containing HEPES buffer and 25 μl of ATPlite 1step solution were mixed, and the luminescence measured after 10-min incubation with the cells (= $luminescence_{t\,=\,0}$).

Reference compound: The IC_{50} value of the reference compound doxorubicin was determined using a separate plate. If the IC_{50} was out of specification (deviation 0.32–3.16 times from the historic average), the assay was invalidated.

Cell growth control: The cellular doubling times of all cell lines were calculated based on the growth of untreated cells at times 0 and 72 h. If the doubling time was out of specification (deviation of 0.5–2.0 times from the historic average), the assay was invalidated.

Maximum signals: For each cell line, the maximum luminescence was recorded after incubation for 72 h without the test compound in the presence of 0.4 % DMSO (= $luminescence_{untreated,\ t\,=\,72\ h}$).

Data analysis of the cancer panel

IC_{50} values were calculated by non-linear regression using IDBS XLfit5 (IDBS, Guildford, UK). The percentage growth after 72 h (%growth) was calculated as follows: 100 % × (*luminescence*$_{t = 72\ h}$ / *luminescence*$_{untreated,\ t = 72\ h}$). This was fitted to the log_{10} compound concentration (conc) by a four-parameter logistics curve: %growth = *bottom* + (*top* - *bottom*) / [1 + $10^{(logIC50\text{-}conc)*hill)}$], where hill is the Hill-coefficient, and *bottom* and *top* the asymptotic minimum and maximum cell growth, respectively, that the compound allows in the assay.

Model prediction and docking simulation

The model structure of human S1PR3 was obtained by using the I-TASSER server (Yang et al., 2015). The server generated two S1PR3 models with high scores using the structures of dopamine D_3 receptor (PDB ID: 3PBL) or β_2-adrenergic receptor-Gs complex (PDB ID: 3SN6) as templates. Both S1PR3 models were processed using the protein preparation wizard implemented in the Schrödinger suite 2017-01 (Madhavi Sastry et al., 2013). The LigPrep tool (Schrödinger, New York, NY, USA) was used to convert docking compounds into protonated 3D structures. To define the binding grid, the receptor grid generation tool was applied based on the predicted orthosteric binding pocket of the model structures. Each compound was docked using the standard precision in Glide (Schrödinger). The structures with the highest score for each compound were selected. Docked structures for ALESIA model 1, CYM-5541, and S1P were obtained using the S1PR3 model calculated based on the structure of the β_2-adrenergic receptor. Docked structure for ALESIA model 2 was obtained using the S1PR3 model calculated based on the structure of the dopamine D_3 receptor.

Pathway analysis

RNA-Seq data was downloaded from CCLE (Ghandi et al., 2019). Mann–Whitney U test (Wilcoxon rank-sum test) was conducted using R software (ver. 4.0, R Development Core Team). Pathway analysis was performed using Metascape (Zhou et al., 2019).

QUANTIFICATION AND STATISTICAL ANALYSIS

Unless otherwise specified, all data plotting and statistical analyses were performed using Prism 6 or 7 (GraphPad Software, La Jolla, CA, USA), and the error bars represent the SEM. Statistical significance was evaluated by one-way ANOVA with independent post-hoc Tukey's multiple comparison test and was defined as a p-value of less than 0.05. To compare two groups, Student's *t*-test and two-way ANOVA were used. In Kaplan-Meier analysis, the log-rank test was used to evaluate the differences in survival among groups. Statistical details of each experiment can be found in the figure legends.